UNIVERSITÀ DEGLI STUDI DI PADOVA

Dipartimento di Fisica e Astronomia *"Galileo Galilei"*

Master Degree in Astrophysics and Cosmology

Final Dissertation

Binary black holes from population III stars

Thesis supervisor:
Prof. Michela Mapelli

Candidate:
Lorenzo Merli

Thesis co-supervisor:
Dr. Filippo Santoliquido
Dr. Giuliano Iorio

Anno Accademico 2021/2022

Contents

Abstract

The properties of population III (pop III) binary systems are still unknown. Nonetheless, those systems are expected to be a relevant source of binary black hole (BBH) mergers that will become observable with the next generation of gravitational waves detectors. In this thesis, we estimate the merger rate density of BBHs with pop III origin and investigate how it is affected by the uncertainties about the star formation rate density (SFRD), initial mass function and distribution of mass ratio, orbital period and eccentricity for pop III binaries. We have calculated the merger rate density by means of the script Cosmo$\mathcal{R}$ate (Santoliquido et al., 2020), coupled with the population synthesis code SEVN (Spera et al., 2019). A total of 64 runs were made. Each run was carried on assuming a different set of prescriptions for the SFRD and for the distribution of binary initial conditions. The results show that the main source of uncertainties is the description of the SFRD. In addition, initial mass function, mass ratio, orbital period and eccentricity distribution affect the merger rate density as they condition the mechanisms of interaction between the system components, consequently influencing the delay time distribution and, more importantly, the merger efficiency.

Chapter 1

Introduction

Increasingly precise measurements of the cosmic microwave background (CMB) (Planck Collaboration, Aghanim, Akrami, & Ashdown, 2020) consolidate our knowledge of the early Universe ($z \sim 1000$): it appears simple, almost homogeneous and manly composed of hydrogen and helium. The local Universe, on the other hand, is filled with complex structures, such as stars and galaxies, hierarchically organized to form the so-called cosmic web. Investigating the transition phase of the Universe from simplicity to complexity is one of the greatest challenges for modern astrophysics and cosmology (Barkana & Loeb, 2001). The formation of the first stars - called population III (pop III) - marks a central milestone in this transition.

In the past decades, intensive observational and theoretical efforts have been made to study the formation, evolution and legacy of those objects. Unfortunately, the observable electromagnetic signals from the high redshift universe ($7 < z < 1000$) are extremely faint or absent across the electromagnetic spectrum, therefore making this era very challenging to study with the instrumentation currently available. For this reason, the development of new observational strategies has gained more and more relevance in recent years.

The first direct detection of gravitational waves (GW) showed a revolutionary way to look at the Universe. On September 14th, 2015, the LIGO GW detectors captured the GW signal from the merger of two back holes (BHs) with masses $M_1 = 36^{+5}_{-4}$ $M_\odot$ and $M_2 = 29^{+4}_{-4}$ $M_\odot$ at redshift $z = 0.09^{+0.03}_{-0.04}$ (Abbott et al., 2016), opening a new era of astrophysical observation. Starting from that groundbreaking event, other GW detectors joined the observational effort - Virgo in 2017, KAGRA in 2020 - and several compact merger events have been observed. The signal from a binary compact object merger carries a huge amount of information about its emitters, therefore it can be used to study its progenitors.

The possibility to use this new observational window to investigate the first stars, observing the mergers of binary black holes (BBHs) formed from this population, was proposed e.g. in (Belczynski, Bulik, & Rudak, 2004) and has been explored since then. The detection horizon for GW instruments currently

operative is $z \lesssim 2$. Thus, we are still blind to the age of the Universe where merger events from pop III black holes are expected to be important ($z \gtrsim 7$) (Kinugawa, Inayoshi, Hotokezaka, Nakauchi, & Nakamura, 2014). Nonetheless, the next generation of gravitational detectors, such as the Einstein Telescope, Cosmic Explorer and LISA, will allow us to observe almost the entire history of complex structures (up to $z \gtrsim 10$) (Punturo, Abernathy, & Acernese, 2010; Amaro-Seoane, Audley, Babak, & Baker, 2017). In order to be prepared for the next observational era, it is extremely important to build reliable theoretical predictions about the properties of the events we expect to detect.

In this work, we will mainly focus on the predicted distribution of BBH mergers across the history of the Universe. To adequately understand the importance of this prediction and the challenges that it poses, it is crucial to have a broader picture on what we know and what is still uncertain about population III formation, evolution and legacy.

1.1 Pop III stars

By definition, population III is a population of stars that existed before the pop I or II we observe today and that were formed in an extremely metal poor environment ($Z \lesssim 10^{-3}\mathrm{Z}_{\odot}$). The existence of pop III had already been hypothesized more then forty years ago (Wagner, 1978; Bond, 1980) [1].

Despite many years of investigation and observational attempts, there is still no direct observation that probes the existence of this population. A conclusive understanding of the properties that characterize pop III stars is prevented by the lack of direct measurements. The knowledge of pop III properties currently available mainly comes from numerical simulations (see e.g. (Greif, 2015)) and can be summarized as follows:

- Pop III stars form from the primordial gas left from the recombination epoch, in the redshift range $z \sim 35 - 7$;
- At formation, they are metal free ($Z \sim 0 - 10^{-3}\mathrm{Z}_{\odot}$);
- Their initial mass function is likely more top-heavy than that of pop I and II stars, with typical masses $\sim 100\ \mathrm{M}_{\odot}$
- Their initial radius is smaller compared to later population with same mass;
- Their lifetime is of the order of few million years;
- They experience negligible mass loss throughout their life;
- They tend to be in binary systems and experience mass transfer with their companion throughout their life;

[1] Early suggestions can be traced back to (Schwarzschild & Spitzer, 1953).

- They tend to experience a violent final phase, either with (1) a core-collapse supernova, (2) A pair instability supernova or (3) a direct collapse, depending on their final mass.
- The path they follow during their final phase determines the impact they have on the surroundings and their contribution on the metal enrichment process of the intergalactic medium.
- The metal enrichment they cause is the factor that ultimately stops their stellar formation at $z \sim 6 - 7$

All these predictions, however, are highly influenced by uncertainties thus they are still under debate. Nonetheless, the improvement of instrumentation and computational power experienced in recent years allows us to constrain them with increasing accuracy.

A population with such properties, may have played a crucial role in shaping the Universe we observe today:

- Pop III stars synthesized the first heavy elements, enabling the formation of later star populations and driving the early metal enrichment of the intergalactic medium (IGM) (Pallottini, Ferrara, Gallerani, Salvadori, & D'Odorico, 2014);
- They are the first strong source of radiation after the CMB, contributing to early ionization and heating of the Universe (Wise et al., 2014);
- They might even provide seeds for super massive black holes (Banik, Tan, & Monaco, 2019).

The aim of this section is to present an introductory picture of the life of population III stars from the mechanisms that drive their formation, to the legacy they left behind at the end of their evolution. We will therefore lay down the model our current understanding of pop III characteristics is based on, the main sources of uncertainties and the influence they have on the resulting pictures.

1.1.1 Star formation

The properties of a star in the zero age main sequence (ZAMS) - i.e. the moment at which nuclear burning starts - are largely determined by the environment that hosts the stellar formation and by the mechanisms that drive the this process. In the case of pop III, this environment is the primordial gas left from the recombination epoch. The initial conditions for the formation process, for this reason, is relatively simple to model and well constrained (detail in the next paragraph). These constraints come from the studies of the CMB, carried on in the context of ΛCDM cosmology (Planck Collaboration et al., 2020). Starting from this framework it is here presented a simplified model for the most important factors that contribute to the star formation.

Cosmological context

Observation of the CMB shows that the Universe at recombination ($z \sim 1000$) was almost perfectly uniform, with spatial perturbations in the energy density and gravitational potential (here called overdesities) of roughly one part in 10^5 (Planck Collaboration et al., 2020). These overdensities - which can be defined as $\delta = (\rho - \overline{\rho})/\overline{\rho}$, where ρ is the local mass density and $\overline{\rho}$ the mean density of the Universe - grow in proportion to the scale factor $a = 1/(1+z)$ as long as $\delta \ll 1$ (Bernardeau, Colombi, Gaztañaga, & Scoccimarro, 2002). Once δ becomes of order unity, the associated region decouples from the expanding background Universe and starts collapsing under its own gravity and virializes, eventually creating dark matter halos.
Once the halos are formed and virialized (so that the potential energy W and the kinetic energy K are related by $W = -2K$), the pressure gradient from the baryon component can delay or stop the collapse. The halos, nonetheless, continue to hierarchically grow in mass, through subsequent mergers of similar mass object. The increasing gravitational pull can eventually overcome the baryonic gas pressure and trigger the halo collapse.

The goal of the next paragraphs is to reach a prediction of the minimum mass required for a halo to successfully collapse to a scale that allows star formation to occur. It is possible to obtain this prediction considering two main aspects, gravitational instability and cooling (Loeb & Furlanetto, 2013), which provide two distinct mass threshold.

Jeans Mass

In first approximation, it is possible to set the boundary between gravitationally stable and gravitationally unstable regimes using the Jeans mass (Jeans, 1902) (Barkana & Loeb, 2001). Considering the halo as a spherically symmetric object, in Newtonian gravity the Jeans mass take the form:

$$M_J = \frac{4\pi}{3}\rho_0 \Big(\frac{\lambda_J}{2}\Big)^3 M_\odot \tag{1.1}$$

where $\lambda_J = c_s\sqrt{\frac{\pi}{G\rho_0}}$ is the Jeans length, ρ_0 is the cosmological background density and c_s is the sound speed in the unperturbed intergalactic medium. When the halo mass $M_h > M_J$, it collapses under the effect of its own gravity since the pressure gradient forces of the gas are not able to balance gravitational pull.

The Newtonian derivation of the Jeans mass, however, is not formally correct since it does not consider expansion of the background. It is possible to carry out the derivation of M_J in a more consistent way using a perturbative approach (Peebles, 1993). Omitting the derivation, the equation of Jeans mass for $z \lesssim 100$ can be written as (Loeb & Furlanetto, 2013):

$$M_J = 4.54 \times 10^3 \Big(\frac{\Omega_m h^2}{0.15}\Big)^{-1/2} \Big(\frac{\Omega_b h^2}{0.022}\Big)^{-3/2} \Big(\frac{1+z}{10}\Big)^{3/2} M_\odot \tag{1.2}$$

where Ω_m is the dimensionless cosmological matter density parameter, h is the value of the Hubble constant in units of 100 km s^{-1} Mpc^{-1} and Ω_b is the dimensionless cosmological baryon density parameter.

In order to obtain a more accurate estimation for the critical mass, it is required to use time-averaged Jeans mass, denoted as the "filter mass" (Gnedin & Hui, 1998), as stability limit. While the Jeans mass declines with cosmic time as the Universe cools, the filtering mass remains roughly constant over a wide redshift interval, $M_F \sim 10^4 - 10^5$ $M_\odot$ for $z \lesssim 100$ (Naoz & Barkana, 2007).

Cooling mechanism

The filtering mass is a reasonable assumption for the first of the two mass thresholds. Above this threshold, the halos enter a state of gravitational instability and start to collapse. Nonetheless, for stars to form inside a minihalo, it is not enough that the gas is gravitationally unstable; it must also be able to cool efficiently (Rees & Ostriker, 1977) . This requirement implies that the energy lost by radiation overcomes the energy released by gravitational contraction, otherwise the collapse will inevitably be stopped. Therefore, to determine the minimum mass of a star-forming minihalo, we must first understand how cooling occurs within primordial gas.

The main products of Big Bang nucleosynthesis are hydrogen ($\sim 76\%$), helium ($\sim 24\%$) and few traces of lithium. Heavier elements - that are responsible for the cooling of star forming clouds in the local Universe - are formed as a consequence of stellar activity and are thereby absent in primordial gas. The lack of these elements generates the necessity for a different mechanism to drive the cooling in an environment composed of isotopes, ions and molecules of hydrogen and helium.

A reasonable approach to identify the dominant cooling mechanism is to investigate the radiatively active chemical species -i.e. the species that are capable to emit and absorb radiation- in the minihalos when it becomes gravitationally unstable. This information heavily depends on the gas temperature inside the minihalos at this stage. We can estimate the typical temperature of a minihalo with mass M_F by assuming the gas is relaxed to a state of viral equilibrium $W = -2K$. Viral temperature is linked to mass and redshift by the relation (Barkana & Loeb, 2001):

$$\begin{aligned} T_{\rm vir} &= \frac{\mu m_p V_c^2}{2k} \\ &= 1.98 \times 10^4 {\rm K} \Big(\frac{\mu}{0.6}\Big) \Big[\frac{\Omega_m}{\Omega_m(z)} \frac{\Delta_c}{18\pi^2}\Big]^{1/3} \Big(\frac{M}{10^8 M_\odot}\Big)^{2/3} \Big(\frac{1+z}{10}\Big) h^{2/3} \end{aligned} \tag{1.3}$$

where μ is the mean molecular weight, m_p is the proton mass, V_c is the circular velocity of the minihalo, k is the Boltzmann's constant, $\Omega_{m(z)}$ is the dimensionless cosmological density parameter evaluated at redshift z and $\Delta_c = 18\pi^2 + 82d - 39d^2$, with $d = \Omega_m(z) - 1$.

According to this formula, the typical temperature of a minihalo with mass M_F is on the order of $T_{\rm vir} = 10^3$ K.

This temperature is too low to have efficient cooling due to atomic hydrogen, which requires $T \gtrsim 10^4$ K (Abel, Anninos, Zhang, & Norman, 1997). Instead, the main source of cooling is expected to be the radiative transitions of molecular hydrogen H_2. This cooling process consists in an H_2 molecule which is first rotationally or vibrationally excited through a collision with another particle and subsequently de-excited, causing the emission of radiation.

To better explain the cooling mechanism and his consequence, it is useful to answer the following questions: how is this molecule formed? How abundant is it in the minihalo? Under which condition is it an effective source of cooling? To answer the first question we consider the most important of the many possible formation channels of H_2 in the early Universe (a more complete list list of them can be found in e.g. (Abel & Haiman, 2000)):

$$\begin{aligned} H + e^- &\rightarrow H^- + h\nu \\ H^- + H &\rightarrow H_2 + e^- \end{aligned} \tag{1.4}$$

Electrons act as a catalyst, therefore H_2 is produced faster and more abundantly in regions rich of e^- (Glover, 2005). Shifting the focus on the abundance of H_2, it is possible to relate it to the gas temperature, as shown in (Tegmark et al., 1997)

$$f_{H_2} \propto T^{1.5} \tag{1.5}$$

where $f_{H_2} = n_{H_2}/n_H$, where n_{H_2} and n_H are the number density of molecular and atomic hydrogen respectively. For $T \sim 10^3$ K, this abundance lies around $f_{H_2} \sim 10^{-4}$ (Tegmark et al., 1997).

The last, and most important, aspect we have to tackle is the necessary condition to have effective cooling via H_2. It is not sufficient for the cooling to be onset, it also has to be strong enough to radiate away the energy released by the gravitational contraction, allowing the collapse to continue. Following (Abel et al., 1997), it is possible to express this problem in terms of the characteristic timescale of the two processes, gravitational contraction and cooling. In this framework, the cooling timescale $t_{\rm cool}$ and the free fall timescale $t_{\rm ff}$ are compared, with the requirement that $t_{\rm cool} \ll t_{\rm ff}$. The equation for free fall timescale - assuming spherical symmetry - is

$$t_{\rm ff} = \sqrt{\frac{3\pi}{32G\rho}}\text{yr} \tag{1.6}$$

where ρ is the density of the halo; whereas we define a cooling timescale as (Glover, 2013)

$$t_{\rm cool} = \frac{1}{\gamma - 1}\frac{n_{\rm tot}kT}{\Lambda}\text{yr} \tag{1.7}$$

where $n_{\rm tot}$ is the total number density of particles, γ is the adiabatic index, k is Boltzmann's constant, T is the gas temperature and Λ is the radiative cooling rate per unit volume.

It is possible to recast the general equation for τ_{cool} (eq. 1.7) in the specific case of H_2 cooling. The details of the derivation can be found in (Tegmark et al., 1997), while the resulting equation reads:

$$t_{\rm cool} = 5 \cdot 10^4 f_{H_2} \Big(\frac{1+z}{20}\Big)^3 \Big(\frac{\delta}{200}\Big) \Big(1 + \frac{10 T_3^{7/2}}{60 + T_3^4}\Big)^{-1} \exp\Big(\frac{512K}{T}\Big) \text{yr} \qquad (1.8)$$

where $T_3 = T/(10^3 \text{K})$, $\delta = (\rho - \overline{\rho})/\overline{\rho}$ as already defined, and the constants result from quantum mechanical calculations of the H_2 collisional excitation rates.

When $t_{\rm cool} \ll t_{\rm ff}$, the gas never becomes pressure supported -i.e. the energy released in the contraction never counterbalances the gravitational pull-, but instead simply collapses at a rate near free-fall. A straightforward calculation (detailed derivation in (Glover, 2013)) shows that this condition is met for a virial temperature of about 1000 K, with little dependence on redshift. Using this information, it is possible to calculate the minimum halo mass required to have efficient cooling. Following (Glover, 2013)

$$M_{\rm cool} = 3.5 \times 10^5 M_\odot \Big(\frac{1+z}{20}\Big)^{-3/2} \qquad (1.9)$$

For $z \gtrsim 40$ the filtering mass is higher than $M_{\rm cool}$. As a consequence, it is not possible to have effective cooling during the collapse and the star formation is prevented above this redshift. On the contrary, for lower z, $M_{\rm cool}$ poses an higher mass threshold with respect to M_F, typically an order of magnitude higher. For instance, in this case we can find halos of mass $M_{\rm cool} > M_{\rm halo} > M_F$ - that are gravitationally unstable but unable to host star formation, for the lack of an effective coolant - and halos of mass $M_{\rm halo} > \max(M_{\rm cool}, M_F)$ that are be able to successfully collapse and cool, thus entering the next phase of star formation. As a result of this discussion, it is possible to assume $M_{\rm cool}$ as the minimum minihalo mass for which star formation is possible. It is important to underline that a different treatment of gravitational collapse and cooling process may lead to a different prediction of the two mass thresholds, consequently to a different minihalo size and and maximum redshift.

Protostellar cloud

To this point, it has been possible to present a few simplified analytical arguments that allow us to follow the collapse process. The last phase of star formation, however, can only be investigated through numerical simulations, as the complexity and uncertainties notably increase (Greif, 2015). A good quantity we can use to track the evolution of the gas through the different stages of the collapse is the number density of hydrogen nuclei n_H, which increases linearly as the contraction continues, whereas the temperature responds in less homogeneous way to the different stages of the collapse.

Indeed, the initial stages of the collapse occur outside the local thermal equilibrium (LTE) and the cooling rate -driven by H_2- goes as $\Lambda_{H_2} \propto n_H^2$ (Bromm, Coppi, & Larson, 2002). The transition from non-LTE to LTE occurs approximately at a density of $n_{H,\rm crit} = 10^4$ cm^{-3}, when the gas has a temperature of

$\sim$ 200K. The cooling time in the LTE regime becomes equal to the free-fall time. At this stage the cooling rate slows down, $\Lambda_{H_2} \propto n_H$, and consequently the halo collapse stalls while the central part of the cloud continues to accrete mass. The central gas cloud eventually accretes enough mass to overcome the Jeans mass limit, which at this characteristic density and temperature is $M_J \sim 100$ $M_\odot$ (Greif, 2015). When this limit is exceeded, the last, almost isothermal collapse of the central gas cloud is triggered.

The characteristic of the collapse is non-trivial. As the density increases, new H_2 formation processes gain relevance, as well as different emission mechanisms arise, since the gas becomes more opaque and the collision between particles becomes more energetic (detailed treatment of mechanisms can be found in (Greif, 2015)).

The last process able to cool the gas is collisional dissociation of H_2. The density at which this mechanism becomes relevant is unclear, but when the process onsets, the collisions between molecules are energetic enough to cause molecular dissociation and decrease the abundance of H_2 (Turk, Abel, & O'Shea, 2009). Following the dissociation of H_2, the temperature rises steeply with an increasing density. At densities $n_H \sim 10^{20}$ cm^{-3} the collapse stalls and an accretion shock forms that heats the gas up to $T \gtrsim 10^4$ K (Yoshida, Omukai, & Hernquist, 2008). This marks the formation of a protostar at the center of the cloud with an initial hydrostatic core of mass $\simeq 10^{-2}$ $M_\odot$.

Accretion

From this point on, the protostellar core starts to accrete mass up to his final value, when radiation feedback eventually terminates accretion in $\sim 10^5$ yr. The initial mass of the hydrostatic core in the case here described is very similar to the core mass we expect in present-day star formation. This detail remarks the importance that accretion process has in determining the mass that the star will posses at the end of the formation process.

As a first approximation, time-averaged accretion rate may be estimated -neglecting radiative transfer effects and fragmentation- as follows (Omukai & Palla, 2003):

$$\dot{M} \sim \frac{M_J}{t_{\rm ff}} \propto T^{3/2} \tag{1.10}$$

where the Jeans mass is evaluated at the density and temperature of the gas, at the moment it becomes gravitationally unstable. If we compare the temperature of the primordial cloud - $T \sim 200$ K as seen in sec. 1.1.1 - and the temperature of the present day star forming regions - where heavy elements cool the gas to $T \sim 10$ K -, we found more than two orders of magnitude of discrepancy. Since the accretion rate is largely responsible for setting the final stellar mass, it is already possible to predict that first stars were much more massive than their present-day analogous. A more accurate description of the accretion process is still under debate and highly, at the present day, uncertain.

It is possible to add a first layer of complexity to this idealized model by accounting for the radiative feedback from the protostellar core. Indeed, the

radiation emitted from the center of the protostar may shut down the accretion flow, hence limiting the amount of mass that the core can accrete and, as a consequence, the final mass of the star.

Some studies, e.g. (Hirano et al., 2014), argued that this process is not particularly important and found the final stellar masses to be in the range $\sim 10 - 1000$ $M_\odot$. In contrast, other studies such as (Susa, Hasegawa, & Tominaga, 2014), found the radiation feedback -in particular from molecular dissociation- to be more influential, lowering the mass range on pop III to $\sim 10 - 100$ $M_\odot$. In ether models, the of initial mass distribution obtained lean towards the formation of massive objects, in other words, the pop III the initial mass function (IMF) is expected to be top-heavy.

Fragmentation

Another crucial and poorly understood aspect that must be taken into consideration is the insurgence of fragmentation during the accretion. Fragmentation can happen in different phases of the star formation. The phase at which fragmentation is triggered determines its end product. (Glover, 2013) suggest that fragmentation can happen even before the formation of the protostellar core, during the initial collapse phase. The relevance of this evolutionary path lies in the fact that it may lead to the formation of wide binaries. Most of the fragmentation process, however, is expected to occur after the first protostar has formed.

If the cloud fragments shortly after the formation of the first protostar, a secondary protostellar core forms and it may accrete a significant part of the surrounding materials before they reach the center of the cloud. In this case the "secondary" star can reach a mass comparable to the one of the central star. Such a situation is explored e.g. in (T. Peters, Klessen, Mac Low, & Banerjee, 2010).

Another possibility is that the accretion disk becomes gravitationally unstable and fragments, thereby creating multiple low mass clumps which can, eventually, merge with the central protostellar core or survive to become lower mass stars. The number of fragments that manages to survive and their typical mass is not clear and strongly depends on the model considered. Early work, e.g. (Abel, Bryan, & Norman, 2000), predicts that the first protostar - formed at the center of the gas cloud - manages to accrete most of the mass, so that each cloud hosts the formation of one, very massive, star. Later simulations (Clark, Glover, Klessen, & Bromm, 2011) find a more efficient fragmentation, that leads the formation of ~ 10 proto-stars per halo of lower mass.

Another implication to keep in mind while discussing this uncertainties is that the way these processes are treated has a particular importance in determining the binary initial condition statistics we will discuss in sec 2.2.1. Note that we have not considered physical aspects -such as rotation of the gas cloud or magnetic fields- that can add even more complexity to the star formation scenario.

Population III.2

So far we have discussed the formation mechanism of the very first stars. We assumed the initial gas to be neutral, with very little preexisting H_2, because it has never been influenced by stellar activity. The stellar population born in this environment can be referred as pop III.1 (McKee & Tan, 2008). However, once the first stars are formed, the initial conditions for other stars immediately becomes more complex.

As we saw in previously, H_2 serves as the main coolant in pop III.1 star formation. In this scenario, the gas can be properly cooled only in the presence of this species. Molecular hydrogen, however, is a very fragile molecule: it can be photo-dissociated by UV photons in the Lyman-Werner band (between 11.26-13.6 eV) (Ciardi, Ferrara, & Abel, 2000). As soon as the first stars formed, they produced a background of UV light, dissociating the H_2 present in the surroundings and suppressing the formation of similar stars in the host and nearby halos. Moreover, the radiation emitted by pop III.1 stars can also ionize the gas, further changing the chemistry inside the halo (Haiman, Abel, & Rees, 2000). For this reasons, later generations of stars, although born in a virtually metal free environment, may follow a very different formation path.

In absence of H_2 cooling, the halo can grow hierarchically without collapsing until it reaches a virial temperature of $T_{\rm vir} \sim 10^4$ K. At this point other cooling mechanisms, such as atomic cooling or HD (Hydrogen deuteride) cooling, can trigger the collapse up to the formation of a protostellar core, where the accretion/fragmentation phase can begin (Loeb & Furlanetto, 2013). The stars formed from this new initial condition can be called pop III.2 stars (McKee & Tan, 2008). It is yet to be understood whether the different cooling process translates to a difference in final stellar masses, or the fragmentation experienced by pop III.1 is efficient enough tho make the two populations almost indistinguishable. Nonetheless, the impact that the first stars have in successive star formation can assume an important role in determining the evolution of the star formation rate. See sec. 2.1.1 for a more detailed examination of this aspect.

1.1.2 Evolution

The moment conventionally attributed to the beginning of the stellar evolution, thus the transition from a protostellar cloud to a star, is the ignition of nuclear burning in the stellar core. As for the formation process, the evolutionary path experienced by population III stars may be remarkably different from the one observed in later population stars. The high masses and the low metallicities typical of pop III are the root of this difference.

Extensive evolutionary models for single stellar evolution of zero metallicity stars -on a wide range of masses $\sim 1 - 1000$ $M_\odot$- can be found e.g. in (Marigo, Girardi, Chiosi, & Wood, 2001; Marigo, Chiosi, & Kudritzki, 2003; Ohkubo, Nomoto, Umeda, Yoshida, & Tsuruta, 2009; Heger & Woosley, 2010; Yoon, Dierks, & Langer, 2012). The most important steps of the single stellar evolution

for of a massive metal free star are introduced in the present section. The model presented is afterwards complemented introducing the mechanism that characterize the evolution in the case of a binary systems.

Single stellar evolution

In the last section, we followed the star formation process up to the birth of a small protostellar core and the onset of the accretion phase. As the accretion continues, the proto-star eventually enters a phase of contraction which induces an internal temperature increase.

ZAMS In massive present-day stars, the energy budget that allows them to stop the contraction is provided by the ignition of the CNO cycle - a set of nuclear reactions that converts hydrogen into helium using C, N, O as mediators - in the stellar core. In newly formed pop III stars, however, carbon, nitrogen and oxygen are absent. In this scenario, the only available process for the helium burning is the proton-proton ($p-p$) chain, a set of nuclear reactions that converts hydrogen into helium without the need for any heavy mediator. Nonetheless, the energy provided by the $p-p$ chain may not be enough to stop the contraction. If this is the case - a behaviour expected for stars with mass $M \gtrsim 20$ $M_\odot$ (Marigo et al., 2001) (Yoon et al., 2012)-, the star continues to shrink and the central temperature continues to rise. The central temperature eventually reaches $T_c \sim 10^8$K, by so allowing the production of carbon via $3-\alpha$ process, a set of nuclear reactions that produces carbon from three helium nuclei.

As a consequence to the first carbon production, the CNO cycle can start contributing to the total energy budget of the star in a significant way. The contraction can finally stop and the stars can enter the hydrogen burning phase (main sequence). This moment is referred a the zero age main sequence (ZAMS). The nuclear burning evolution from this point on can proceed following a similar path to the well known pop I/II stars.

The ignition of the $3-\alpha$ process is a noteworthy moment in the stellar evolution since it marks the beginning of the production of elements heavier than helium (metals) in the stellar core, previously absent in the star and in its surroundings.

As a consequence of the longer contraction phase, pop III stars at ZAMS are expected to have smaller radius (in the order of $\sim 10^0 - 10^1$ $R_\odot$ (Ohkubo et al., 2009)(Windhorst et al., 2018)[2]) and higher temperature (effective temperature in the order of $10^4 - 10^5$ K (Ohkubo et al., 2009)(Windhorst et al., 2018)) with respect to later generation, metal rich counterparts with comparable mass (Baraffe, Heger, & Woosley, 2001).

Lifetime An aspect of stellar evolution that pop III shares with present-day massive stars, is their very short lifetime. As a first approximation, we can

[2]The mass range considered in (Ohkubo et al., 2009) and (Windhorst et al., 2018) is $1-1000$ $M_\odot$

indeed relate the nuclear burning timescale -we limited our treatment to the hydrogen burning timescale (τ_h), the largely dominant phase of a stellar evolution- solely to the stellar mass. The models available on this timescales (Marigo et al., 2003) show how τ_h decreases at larger masses, until it flattens out towards the nearly constant value $\tau_H \sim 2 \times 10^6$ yr for $M \gtrsim 0.5 \times 10^3$ $M_\odot$.

As "order of magnitude treatment", we can model this behaviour starting from the definition of H-burning timescale $\tau_H \propto M/L$ and the mass-luminosity relation, that can in general be expressed as $L \propto M^\eta$ (Kippenhahn & Weigert, 1994), so that the relation between timescale and mass is $\tau_H \propto M^{1-\eta}$. In this formalism, it is possible to study the exponent η as a function of the stellar mass (Marigo et al., 2003; Windhorst et al., 2018). For lower mass stars -in range $\sim 1 - 100$ $M_\odot$- the exponent is extrapolated from observable population and takes the value of $\sim 3 - 3.5$. At higher mass -$\sim 100 - 1000$ $M_\odot$- the exponent is expected to decrease gradually to become $\eta \sim 1$, causing τ_h to be mass-independent for very massive stars (Marigo et al., 2003) (Windhorst et al., 2018).

Mass loss Even if a star enters its main sequence with a very high mass, the amount of mass it has conserved at the end of his life - and subsequently that can potentially convey into a compact object - is determined by the amount of mass it loses during the evolution. For this reason it is crucial to understand the mass loss mechanism experienced by pop III stars throughout their life.

Looking at massive stars observable in the local Universe, the main cause of mass loss during main sequence is the radiative stellar wind. The radiative wind is indeed extremely relevant in this later population star, and it can thus induce a huge mass loss from the external stellar layer. Nevertheless, such a wind is driven by line emission of heavy elements. Pop III stars, as already pointed out, are, on the other hand, virtually free of heavy elements, with the exception of the metals produced via nuclear burning in the core. This suggests that the dominant mass loss mechanism in pop III stars requires a different prescription from the one used for their metal-rich counterparts.

An extensive treatment of the mass loss by stellar wind in massive, metal free stars has been carried on e.g. in (Kudritzki, 2002) and (Krtička & Kubát, 2006). These models focus on the dependence of the radiative force on metallicity and temperature in stars mainly composed by H and He and concluded that, for the metallicities typical in pop III, the stellar wind is very weak and consequently lead to a negligible amount of mass loss. Following (Kudritzki, 2002), it is possible to present an analytic argument to justify this conclusion. According to this work, the mass loss rate can be expressed as a function of effective temperature, luminosity and metallicity. For $\gtrsim 100$ $M_\odot$:

$$\log \dot{M} = q_1([Z]_{\min})^{0.5} + Q_{\min} M_\odot \, \mathrm{yr}^{-1} \tag{1.11}$$

where

$$[Z] = \log(Z/Z_\odot), \quad q_1 = Q_0 - Q_{\min}(-[Z]_{\min})^{-0.5},$$

Z is the metallicity, the quantity $[Z]_{\min}$, $Q_{\min}$ and Q_0 are expressed as polynomial functions of the luminosity

$$y = a_0 + a_1\tilde{L} + a_2\tilde{L}^2$$

where $\tilde{L} = \log(L/L_\odot) - 6$, $y = [Z]_{\min}, Q_{\min}, Q_0$, and the coefficient a_1, a_2, a_3 are tabulated (Table 3 in (Kudritzki, 2002)) and depend on the effective temperature. As a qualitative example, following this calculation, a star with a mass of ~ 100 $M_\odot$ returns in the interstellar medium a mass $\lesssim 0.02$ $M_\odot$, a negligible amount. Other researches, e.g. (Maeder & Meynet, 2000), investigate the mass loss driven by the stellar rotation, but the results show that the contribution is even smaller that the mass lost via stellar wind.

To summarize the outcome of the single stellar evolution just presented, pop III is a population of very massive, hot and metal free stars that live only few million years and menage to retain most of his mass throughout their life.

Binary evolution

It is not exhaustive to just consider single stellar evolution to understand the evolutionary path of a pop III stars: it is necessary to account also for binary interaction. Despite early works (Ripamonti & Abel, 2004) deem the formation of pop III binary systems unlikely because of ineffective fragmentation process, more recent studies (Stacy & Bromm, 2013) suggest that a consistent fraction of pop III stars are formed and evolve in binaries, with a binary fraction at least as high as the one of present-day massive stars ($f_{\rm bin} \sim 0.5 - 0.7$ according to (Sana et al., 2012, 2013)). Therefore, in recent investigations, pop III binaries are expected to be abundant and extremely relevant to understand the legacy of pop III stars (Kinugawa et al., 2014; Tanikawa, Chiaki, Kinugawa, Suwa, & Tominaga, 2022).

The presence of a companion can have an enormous influence on the life of a star: the components in a system can exchange and lose mass and angular momentum through a variety of mechanisms that can, eventually, lead to the coalescence or to the disruption of the binary. The mechanisms that characterize binary evolution have been widely studied in the general case (Hurley, Tout, & Pols, 2002; Dominik et al., 2012, 2013) and in the peculiar case of pop III stars (Kinugawa et al., 2014; Belczynski et al., 2017; Inayoshi, Hirai, Kinugawa, & Hotokezaka, 2017). The aim of this section is therefore to present an introductory treatment of the most influential binary interactions, with a particular attention to the consequences they have on the coalescence timescale.

Mass transfer and Roche lobe overflow The most relevant event that characterizes the evolution of a binary system is the exchange of mass, and consequently momentum, that may happen between the system components. In a binary system, the two stars rotate in an elliptical orbit around their common center of mass. Each star has a mass M_i and angular momentum $J_i = M_i a_i^2 \omega_{\rm orb}$, where $\omega_{\rm orb}$ is its angular velocity and a_i is its distance from the

center of mass. Matter can escape the gravitational field of one star -carrying away mass and angular momentum- to be then accreted by the companion or lost in the environment.

A first possibility that may be taken into consideration is that this mass transfer occurs via stellar wind. This process operates as follows: one of the stars in the binary loses mass due to stellar wind and, subsequently, part of this mass is captured by the gravitational field of the companion and accreted by it. The scenario presented, however, is not effective for pop III systems since - as illustrated previously - the amount of mass expelled via stellar wind is negligible for pop III stars.

Therefore, the focus needs to be shifted toward a different mass transfer mechanism: The Roche lobe overflow (RLOF). This mechanism is triggered when at least one of the two stars fills the Roche lobe, i.e. $R_i > R_{L,i}$, where $R_i,\ i = 1, 2$ is the radius of of the stars and the Roche lobe $R_{L,i}$ is defined as the equipotential region around the star i inside which the material is gravitationally bounded to that star. According to (Eggleton, 1983), $R_{L,i}$ assumes the form

$$R_{L,1} = a\frac{0.49q^{2/3}}{0.6q^{2/3} + ln(1 + q^{1/3})} \tag{1.12}$$

where $q = M_1/M_2$ and a is the orbital separation. $R_{L,2}$ can be calculated similarly using $q = M_2/M_1$. The condition of RLOF can be met either (1) because of the expansion that one of the stars in the system undergoes as consequence of its nuclear evolution or (2) because of the contraction of the orbit caused by the loss of angular momentum, e.g. via tidal effects or GW emission.

When a star fills the Roche lobe (hereafter called donor or primary), the outer part of the envelope is free to transit toward the companion (the accretor or secondary). Part of this material is then accreted by the companion while the other part is lost in the environment, causing a net loss of mass and angular momentum in the system. Depending on the reaction of the binary system to the mass transfer, a range of possible scenarios unfolds. Following (Webbink, 1984) it is possible to distinguish these scenarios by means of a stability criterion, constructed with the radius-mass exponents ζ.

$$\zeta_s \equiv \frac{d\ln R_1}{d\ln M_1} \qquad \zeta_L \equiv \frac{d\ln R_{L,1}}{d\ln M_1} \tag{1.13}$$

where ζ_s is the radius-mass exponent for the donor star and ζ_L is the radius-mass exponent for its Roche lobe. The comparison between these two quantities determines whether the response of the stellar radius to mass transfer is more or less rapid than the response of its Roche lobe to the same mass transfer. The result of this comparison often depends on whether the donor envelope is convective or radiative, with convective envelope favouring the unstable mass transfer (Ivanova et al., 2013).

Stable Mass transfer If $\zeta_L \leq \zeta_s$ the mass transfer is stable. In this case, the stellar radius of the donor does not manage to grow above the Roche lobe,

at least until the nuclear evolution causes a further expansion (Webbink, 1984). The only net loss of angular momentum caused by stable mass transfer is related to the fraction of mass lost by the donor that is not captured by the accretor. Hence the semi major axes of the system is almost unaffected and the system is expected to survive the Roche lobe overflow phase and continue on its evolutionary path (Tanikawa, Yoshida, Kinugawa, Takahashi, & Umeda, 2020).

Common Envelope If $\zeta_L > \zeta_s$ the mass transfer is unstable. In this scenario the stellar radius of the donor continues to grow beyond the Roche lobe causing a more violent mass transfer and a contraction of the orbit due to gas friction. If the donor enters the common envelope without a well developed "core-envelope" structure, the system is not able to survive the violent mass transfer and orbit contraction and the therefore merges, becoming a single star. This outcome is verified when the common envelope is triggered while the donor is still in main sequence or right after, in the Hertzsprung gap (Kinugawa et al., 2014). On the other hand, if the donor have already formed a solid a core-envelope structure, the system can successfully enter the common envelope (CE) phase (Paczynski, 1976). The most frequent CE scenario involves a giant donor and a main-sequence accretor (Hurley et al., 2002), hence we assume this case for our treatment.

When CE is triggered, the envelope of the primary rapidly swallows the companion, so that we can consider the system composed of the donor core and the secondary star, which orbit around each other surrounded by an envelope. The friction exerted by the gas of the envelope on the system's components causes a rapid shrinking of their orbit and a transfer of their orbital energy into thermal energy of the envelope.

There are two outcomes for this process (Webbink, 1984). (1) In the first scenario , in-spiral can is stopped when the energy released by the contraction of the orbit overcomes the binding energy of the envelope, causing its compete expulsion. Following this path, at the end of the CE phase the system becomes a close binary composed of a naked core and a main sequence star. Moreover, this scenario opens the possibility for the system to undergo a second CE when the secondary in turn becomes a giant. (2) In contrast, if the the energy released does not successfully eject the envelope, the in-spiral is not halted and the contraction continues until the system merges inside the envelope. It is possible to formulate an analytical argument to distinguish these two scenarios comparing the orbital energy lost during the in-spiral and the binding energy of the envelope (Webbink, 1984)

$$\Delta E_{\rm orb} = \frac{GM_{c,1}M_2}{2a_f} - \frac{GM_1M_2}{2a_i}, \quad E_{\rm bind} = \frac{GM_1M_{\rm env,1}}{\lambda R_1} \tag{1.14}$$

where $M_{c,1}$ and $M_{env,1}$ are the core and the envelope primary mass respectively, a_i and a_f are the semi major axis before and after the the shrinking and λ is a parameter that depends on the property of the envelope. In this framework the system can survive if the fraction of orbital energy that is transferred to

the envelope - $\alpha\Delta E_{\rm orb}$, where α is the efficiency factor of energy conversion - overcomes the binding energy $E_{\rm bind}$ before the objects are too close to each other. We can estimate the final orbital separation using the equation

$$\alpha\Big(\frac{GM_{c,1}M_2}{2a_f} - \frac{GM_1M_2}{2a_i}\Big) = \frac{GM_1M_{\rm env,1}}{\lambda R_1} \tag{1.15}$$

so that if $a_f > R_{c,1} + R_2$ the envelope are ejected before the system merges and a_f becomes the new semi major axes. A very similar situation can be found if both the stars are giants. In this case the system only survive if the envelope of both star is expelled, thereby creating a close binary of naked cores. The values of α and λ are estimated via sophisticated numerical simulations and their resulting values are close to unity (Hurley et al., 2002; Kinugawa et al., 2014).

An accurate prescription for Roche lobe stability and common envelope - and especially its application in the case of pop III stars- is nonetheless still under debate.

The study from (Marchant et al., 2021) affirm that binaries only survive common envelope evolution if the unstable the mass transfer phase happens after the formation of a deep convective envelope, while in all cases where binary interactions is initiated with a radiative envelope, the systems is unable to expel the outer envelope and inevitably merges. Pop III stars - contrary to pop I/II stars which tend to experience a convective red super giant phase - are expected to end their evolution as blue super giants with radiative envelope. They, indeed, present a convective envelope only in the very late stages of their evolution and only for $M_{\rm ZAMS} \gtrsim 50$ M$_\odot$ (Marigo et al., 2001; Kinugawa et al., 2014; Inayoshi et al., 2017). By allowing only these stars can to successfully survive a CE phase, (Inayoshi et al., 2017; Tanikawa et al., 2020) reach the conclusion that a consistent fraction of all pop III binaries experiences stable mass transfer during their evolution. In contrast to that, (Belczynski et al., 2017) allows for both convective and radiative envelope to enter and possibly survive a CE phase, finding that most of the binaries experience a common envelope in one or more points of their life.

Gravitational Wave Decay The effect of binary interaction extends even beyond the nuclear life of the system, affecting the fate of the compact remnants binary formed at the end of the system evolution. Indeed, even without expiring strong mass transfer events, a binary can still lose angular momentum and orbital energy by the emission of gravitational waves. Using the formalism described by (P. C. Peters, 1964), it is possible to write the equations for the change of angular momentum, semi major axis and eccentricity as

$$\frac{\dot{J}}{J} = -\frac{32G^3M_1M_2(M_1+M_2)}{5c^5a^4}\frac{1+\frac{7}{8}e^2}{(1-e^2)^{5/2}}, \tag{1.16}$$

$$\frac{\dot{a}}{a} = -\frac{64G^3M_1M_2(M_1+M_2)}{5c^5a^4}\frac{1+\frac{73}{24}e^2+\frac{37}{96}e^4}{(1-e^2)^{7/2}} \tag{1.17}$$

and

$$\frac{\dot{e}}{e} = -\frac{304 G^3 M_1 M_2 (M_1 + M_2)}{5 c^5 a^4} \frac{1 + \frac{121}{304} e^2}{(1 - e^2)^{5/2}}. \tag{1.18}$$

Therefore, the gravitational waves emission causes a loss on angular momentum and a contraction of the orbit. As a shrinks, the mechanism is even more effective - as the three equations are $\propto a^{-4}$ - and the system keeps shrinking up to coalescence. Integrating the equation 1.17 it is possible to derive the timescale in which the binary will reach coalescence. Assuming a system with initial separation a_0 and initial eccentricity $e_0 = 0$ for simplicity, the coalescence time assumes the form

$$t_{\rm GW} \simeq 10^{10} \Big(\frac{a_0}{16 R_\odot}\Big)^4 \Big(\frac{M_1}{10 M_\odot}\Big)^{-1} \Big(\frac{M_2}{10 M_\odot}\Big)^{-1} \Big(\frac{M_1 + M_2}{10 M_\odot}\Big)^{-1} yr \tag{1.19}$$

This equation has a notable importance in the context of this thesis: by linking t_{coal} to the mass and the semi major axis of the system, it shows the influence that evolutionary events, such as stable mass transfer and common envelope, have on the possibility for the system to merge in a specific time and, as a consequence, on the distribution of mergers across the cosmic time.

A number of additional binary interactions can be taken into account, such as tidal effect or magnetic field interaction. Nonetheless, detail treatment of these mechanisms have been omitted since their impact on pop III binary evolution is analogous to the one studied for later population stars (Kinugawa et al., 2014).

1.1.3 Final fate

In order to study the compact remnants generated form pop III stars it is crucial to understand the final fate those stars encounter at the end of their evolution.

Throughout its life, a star manages to counterbalance the gravitational pressure via the nuclear fusion of increasingly high mass elements. When the stellar core runs out of nuclear fuel to burn, the star is unable to sustain its structure and collapses. The consequence of the collapse can be really violent for massive stars, often triggering a supernova (SN) explosion and resulting either in the formation of a compact object or in the complete destruction of the star.

Several attempts to investigate the mechanisms that drive this last evolutionary phase and its outcome can be found in literature (Fryer, 1999; Heger, Fryer, Woosley, Langer, & Hartmann, 2003; Belczynski, Bulik, et al., 2010; O'Connor & Ott, 2011; Fryer et al., 2012; Woosley & Heger, 2015). The prescription described in these models discriminates among different possible scenarios, depending on the stellar mass and the core mass at the onset of collapse. In the case of pop III stars the amount of mass loss during the stellar evolution is negligible. It is therefore reasonable to assume the final mass to be equal to the initial mass, and consequently to treat the possible final fate as function of the ZAMS mass.

The expected outcomes for different ZAMS mass are displayed in fig. 1.1 and can be summarize as follow:

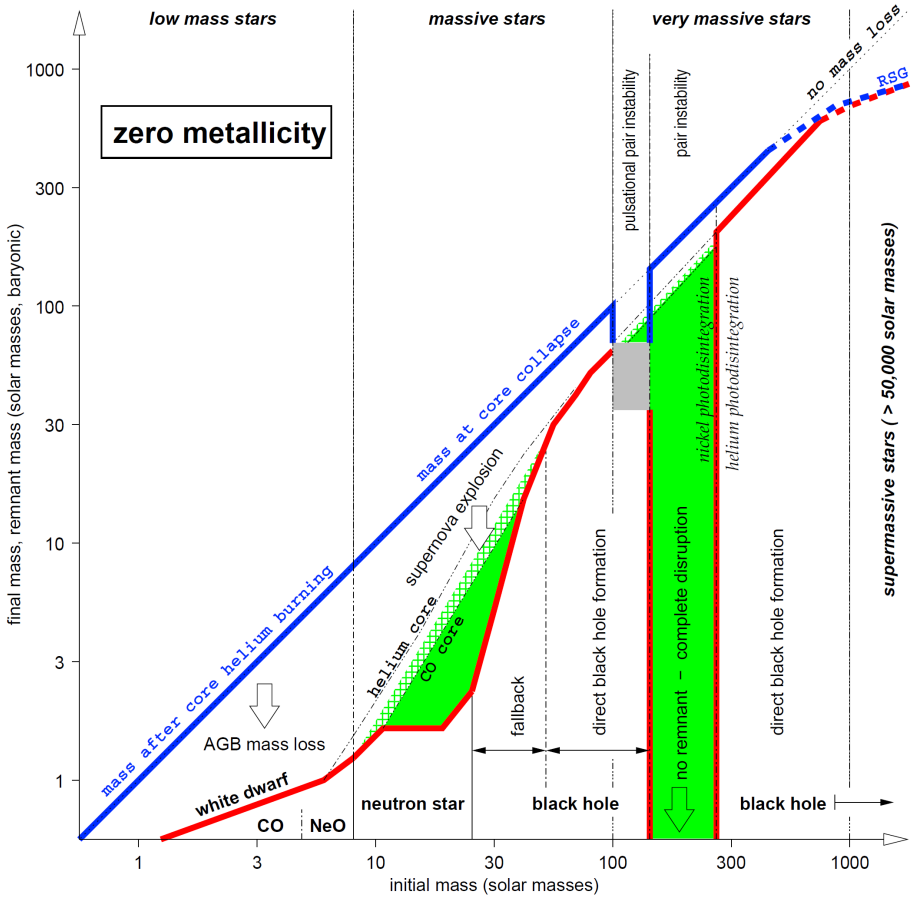

Figure 1.1: Final fate of pop III stars as function of initial mass. The blue line is the stellar mass at time of final explosion/remnant formation and is almost always equal to the initial mass (dotted line). The red line is the remnant mass and the green fill and hatching is the metal released. Source: (Heger, Woosley, et al., 2003).

10 $M_\odot \lesssim M_{\mathrm{ZAMS}} \lesssim$ 40 $M_\odot$: Core-collapse Supernova Pop III stars with initial masses below $\sim$ 40 $M_\odot$ follow a similar fate to later population stars (Heger, Woosley, et al., 2003). In this scenario the collapse is successfully halted by neutron degeneracy and nuclear force, causing the infalling material to "bounce back" with an energetic shock that gives birth to a SN explosion (type II SN) while the core is conveyed into a compact object (a detailed treatmentof this scenario can be found e.g. in (Woosley & Weaver, 1995)). Part of the material initially ejected does not reach the escape velocity and thus falls back into the collapsing core and is finally accreted by the new born compact remnants. Predictions about the compact remnant mass heavily depend on the model used

to describe the SN explosion. Nonetheless, a consistent fraction of the total mass is expected to be lost SN explosion, leaving a relatively low mass remnants, up to ~ 10 $M_\odot$ (Fryer et al., 2012; Belczynski, Bulik, et al., 2010).

40 $M_\odot \lesssim M_{\mathrm{ZAMS}} \lesssim$ 100 $M_\odot$: Direct collapse For metal-free star above ~ 40 $M_\odot$ the gravitational collapse is not stopped and a successful SN shock can not be launched (Fryer, 1999; Heger, Fryer, et al., 2003). Under this condition the entirety of the material composing the star is transferred to the resulting BH with virtually no mass ejected into the environment.

100 $M_\odot \lesssim M_{\mathrm{ZAMS}} \lesssim$ 140 $M_\odot$: Pulsational Pair instability When a star possesses a mass of at least $\sim$ 100 $M_\odot$, it encounters the electron-positron pair creation instability (or pair instability) after central carbon burning (Woosley & Weaver, 1986; Heger, Woosley, et al., 2003; Baraffe et al., 2001). This phenomenon leads to a violent contraction followed by the explosive ignition of oxygen and silicon burning. If the stellar mass is below 140 $M_\odot$, the energy released in the explosion manages to stop the contraction but is not enough to disrupt the entire star. In this scenario, the process is repeated, causing the ejection of the hydrogen envelope and part of the helium core, over the cycles of contraction and expansion (pulsation). The pulsation ends when the star finally loses enough mass to enter the mass regime of direct collapse and thus becomes a BH.

140 $M_\odot \lesssim M_{\mathrm{ZAMS}} \lesssim$ 260 $M_\odot$: Pair instability Supernova If the stellar mass exceeds 140 $M_\odot$, the energy released after the first contraction due to the pair instability is sufficient to completely disrupt the star in a extremely energetic SN explosion (Heger, Woosley, et al., 2003). In this case no remnant is created, as the entirety of the stellar material is ejected into the surroundings.

$M_{\mathrm{ZAMS}} \gtrsim$ 260 $M_\odot$: Direct collapse Finally, at even higher masses the photo-disintegration of the particles that compose the core prevents the collapse from being stopped and reversed, so that it continues to directly generate a BH without any ejection of metals in the interstellar medium (Inayoshi, Kashiyama, Visbal, & Haiman, 2016). The remnants originated in this scenario are exported to be very massive ($M \gtrsim 100$ $M_\odot$).

Together with the influence on single stellar evolution, the final fate of the stars can also impact binary evolution (Kinugawa et al., 2014). The most relevant scenario in this context happens when a binary component ends his life in a core collapse supernova. The compact object formed by this events receives a velocity kick owning to the asymmetry of the explosion. The consequence of the kick can be the disruption of the binary or the drastic modification of its semi major axis and eccentricity. The effect of the kick on Neutron stars has been explored e.g. in (Lyne & Lorimer, 1994) and (Hobbs, Lorimer, Lyne, & Kramer, 2005), whereas the impact of this phenomenon on BHs remains still

poorly understood. In addition to this aspect, the evolutionary path of the system is also affected by the loss of mass and angular momentum, carried away during the SN explosion.

End of pop III star formation

The last aspects discussed in this introduction on pop III characteristics are the conditions and the processes that mark the end of pop III star formation, a topic that is still very controversial and poorly understood (Greif, 2015). In first approximation, it is nonetheless possible to to summarize the requirements for the end of pop III star formation into a single condition on the mean metallicity of the intergalactic medium (IGM). The threshold value of Z - above which massive and metal free (pop III) stars are no more allowed to form - can vary depending on the star formation model, in particular on the role of dust and background radiation in the cooling process (Ciardi & Ferrara, 2005). It is reasonable to assume as reference value $Z_{\rm cr} \sim 10^{-5\pm1}$ $Z_\odot$ (Schneider, Ferrara, Natarajan, & Omukai, 2002).

The focus must then be shifted towards the mechanisms that enrich the IGM of metals. The only objects capable of producing metals in the high redshift universe are pop III stars. For this reason, the cause of metal enrichment in that era is recognized to be pop III stellar activity and the injection of metal rich material into the surroundings it produces. The mechanism that lead to the creation of the compact remnants, in particular, has a dominant role in determining the contribution of a star in this enrichment process, whereas the materials expelled with mass loss and the binary interactions provide a subdominant contribution.

Pair instability supernovae are an extremely efficient source of metal enrichment and are expected to be the driver for metallicity evolution, since they eject the entirety of their metallic core in the environment. For core collapse supernovae, on the other hand, the feedback is less abundant and less metal rich: only the outer layers are expelled while the core survives to be conveyed into the compact remnant. Finally, the stars that experience direct collapse provide a negligible feedback as all of their stellar mass is accreted into the BH. Owing to the local nature of these enrichment phenomena, the metallicity of the medium is expected to be very inhomogeneous. For this reason, even if the mean metallicity is expected to reach the critical value at $z \sim 7$ (Pallottini et al., 2014; Jaacks, Finkelstein, & Bromm, 2019), at $z \sim 15$ pop III star formation is already believed to be subdominant (Yoshida, Bromm, & Hernquist, 2004) and there are prediction of "pockets" of pop III formation that survive up to $z \sim 2.5$ (Schneider, Ferrara, Salvaterra, Omukai, & Bromm, 2003; Tornatore, Ferrara, & Schneider, 2007) (in the most optimistic case, even to $z = 0$(Liu & Bromm, 2020b)).

As a side note, it can be highlighted that feedbacks from pop III stars (chemical, mechanical and radiative) are extremely important observational tools that can be used to probe the characteristics of pop III stars (Ciardi & Ferrara, 2005). The chemical feedback from the SNe explosions, in particular, can provide a constraint on pop III initial mass function (sec. 2.2.1) through the observation

of chemical enrichment pattern left by the SNe events (Karlsson, Johnson, & Bromm, 2008): the pair-instability SNe mainly produce elements with an even nuclear charge and almost no neutron-capture elements, while core-collapse SNe display a characteristic enhancement of α-elements.The statistical recurrence of each type of SN types can thus be investigated through the observation of chemical abundance patterns.

1.2 GW from pop III binaries

The importance conferred to pop III star in the context of gravitational wave astrophysics has significantly grown in recent years. The possibility that binaries of pop III star remnants could be a contributing source of gravitational wave events, detectable with current of forthcoming instrumentation, has been considered by a number of authors (Kulczycki, Bulik, Belczyński, & Rudak, 2006; Kinugawa et al., 2014; Hartwig, Volonteri, et al., 2016; Inayoshi et al., 2016; Kinugawa, Miyamoto, Kanda, & Nakamura, 2016; Belczynski et al., 2017; Liu & Bromm, 2020a; Kinugawa, Nakamura, & Nakano, 2020; Tanikawa et al., 2020; Liu, Meynet, & Bromm, 2021; Kinugawa, Nakamura, & Nakano, 2021a; Tanikawa, Chiaki, et al., 2022). The purpose of the present section is to explore the reason why GWs from pop III stars are so relevant in this new field of astrophysics as well as briefly expose the contribution that the thesis here presented can provide to the discourse.

The peculiarities that distinguish the gravitational waves signal from the much more exploited electromagnetic signal make this observational window particularly suitable for investigating the Universe at higher redshift:

- while the EM radiation decays as d^{-2} with the distance, the GW intensity stales as d^{-1}, hence the detection horizon for GW signals can be more effectively pushed toward higher z with an increase of detectors sensitivity (Sathyaprakash & Schutz, 2009);
- the universe is transparent to GW, i. e. there is no absorption or reflection event in the journey from the emitter to the receiver;
- only "extreme" astrophysical events - like compact object mergers - are capable of generating GW signals strong enough to be detectable by present and near-future instrumentation, hence the GW spectrum is not "polluted by minor events" from stellar or IGM activity in the foreground;
- binary compact systems formed in high redshift universe can survive and slowly in-spiral for billions of years (P. C. Peters, 1964), hence - even if the system's progenitors are long extinguished - merger events are distributed across the cosmic time and they might also occur in the local Universe.

In addition to that, the detection of compact binary mergers with pop III progenitors is favoured by the properties of those systems: the amplitude of a GW

signal from a binary merger, indeed, is proportional to the 5/6 power of the chirp mass of the merging system, defined as

$$M_{\rm chirp} = \frac{(M_1 M_2)^{3/5}}{(M_1 + M_2)^{1/5}} \tag{1.20}$$

where M_1 and M_2 are the mass of the compact components of the binary. Higher mass systems can thus produce stronger GW signals (Sathyaprakash & Schutz, 2009). This is relevant since, as highlighted in the previous section, pop III binaries tend to generate massive compact systems due to high initial masses and suppressed mass loss (Heger, Fryer, et al., 2003). From all the considerations done, it follows that merger events from compact pop III systems are expected to generate strong GW signals, distributed along the cosmic time, that are likely to be detected by future - or even present - detectors (Kinugawa et al., 2014, 2021a).

In particular, the relevance of pop III merger events in the modern scientific discourse is connected to their distribution over the cosmic time, called merger rate density (MRD). Investigating this distribution, however, is a challenging task due to its dependence on the largely unconstrained pop III formation history and binary statistics (Liu et al., 2021) (such as the probability distribution function of masses, orbital period and eccentricity, details in chap. 2). Unfortunately, it is difficult to reduce the uncertainties on these aspects without direct observations of pop III stars, and for this reason investigations of MRD have to rely on previous theoretical studies. In literature, several model proposals can be found to describe the properties of pop III binaries (Clark et al., 2011; Greif et al., 2012; Stacy & Bromm, 2013; Liu et al., 2021). The predictions from these studies, however, exhibit significant discrepancies often due to a different treatment of the pop III star formation and evolution, as better argued later in the next section.

Studying the effects that different assumptions on formation history and binary statistics have on pop III MRD is crucial to build a more complete understanding of this function and thus to correctly interpret the existing observation from LIGO-Virgo collaboration (The LIGO Scientific Collaboration et al., 2021) and to build a observational strategy for the future generation of GW detectors (Kinugawa et al., 2014; Liu & Bromm, 2020a), such as Einstein telescope (Punturo et al., 2010), Cosmic explorer (Reitze et al., 2019), Lisa (Robson, Cornish, & Liu, 2019). For this reason, the work presented on this thesis investigate the merger rate density of BBHs with pop III origin, focusing on how it is affected by the uncertainties about the star formation history and the distribution of binary initial conditions.

Chapter 2

Methodology

The merger rate density can be defined as the number density of merger events as a function of redshift. In our implementation, the MRD is obtained as a combination of star formation rate density (SFRD), binary merger efficiency and time delay from formation of stars to system merger, (see eq. 2.4). The SFRD can be defined as the quantity of star formation occurring - in mass unit - per unit time per unit volume at a specific redshift (Jo et al., 2021), i.e. it describes the evolution of the star formation in time. The delay time ($t_{\rm del}$), on the other hand is the time elapsed from the formation of the binary star to the merger of the two compact objects and, finally, the merger efficiency (η) is the ratio between the total number of mergers and the total initial mass.

The dependence on the formation history is, therefore, explicit in the calculation of the MRD, while the dependence on the binary initial conditions is implicit in the binary merger efficiency and time delay. These two quantities are indeed estimated from compact binary catalogues generated with a population syntheses code, which uses the binary initial condition distributions as input of the simulation.

The investigation done in this thesis on the MRD has been carried out adopting two separate scripts, both customized to account for the peculiar characteristics of population III.

The calculation of the MRD has been performed using the code Cosmo$\mathcal{R}$ate, from (Santoliquido et al., 2020). In order to operate the calculation, the code necessitates an input catalogue of binary objects. For this reason, Cosmo$\mathcal{R}$ate has been paired with the population syntheses code SEVN (Spera et al., 2019) to generate all the binary catalogues utilized by the different runs of the script.

Here the main features of Cosmo$\mathcal{R}$ate and SEVN are presented with a particular focus on the changes we implemented for our work.

2.1 CosmoRate

The original goal of CosmoRate (Santoliquido et al., 2020) is to calculate the MRD of pop I/II stars both in the isolated and dynamical scenario (i.e. from isolated binary systems or dynamical interactions inside a stellar cluster). It does that by combining the SFRD and the metallicity evolution - from (Madau & Fragos, 2017) - with the information about the stellar evolution provided by an input catalogue of binary compact objects, generated with a population syntheses code.

The equation it uses to calculate the merger rate density is:

$$\mathcal{R}(z) = \frac{d}{dt_{\rm lb}(z)} \int_{z_{\rm max}}^{z} \psi(z') \frac{dt_{\rm lb}(z')}{dz'} dz' \int_{Z_{\rm min}(z')}^{Z_{\rm max}(z')} \eta(Z) \mathcal{F}(z', z, Z) dZ \; Gpc^{-3} yr^{-1} \tag{2.1}$$

where $t_{\rm lb}(z)$ is the look-back time at redshift z (calculated using the cosmological parameter from (Planck Collaboration et al., 2016)), $\psi(z')$ is the SFRD at redshift z', $Z_{\rm min}(z')$ and $Z_{\rm max}(z')$ are the minimum and maximum metallicity of stars formed at redshift z', $\eta(Z)$ is the merger efficiency at metallicity Z and $\mathcal{F}(z', z, Z)$ is the fraction of compact binaries that form at redshift z' from stars with metallicity Z and merge at redshift z, normalized to all CBs that form from stars with metallicity Z.

The script uses the information about the masses of the two compact objects, the delay time and the metallicity of the progenitor stars contained in the input catalogues to calculate $\eta(Z)$ and $\mathcal{F}(z', z, Z)$. In particular, the merger efficiency is defined as

$$\eta(Z) = \frac{\mathcal{N}_{\rm TOT}(Z)}{M_{\rm TOT}(Z)} \tag{2.2}$$

where $\mathcal{N}_{\rm TOT}$ is the total number of CBs that merge within a Hubble time ($t_{\rm del} \lesssim 14 Gyr$) and form from stars with metallicity Z, and $M_{\rm TOT}(Z)$ is the total ZAMS mass simulated with metallicity Z. Both these quantities are taken from the input catalogues and then corrected for the binary fraction ($f_{\rm bin}$) and the fraction of IMF from which the smiling is made ($f_{\rm IMF}$), so that $\eta(Z) = (\mathcal{N}_{\rm bin,sim}(Z)/M_{\rm TOT,sim}(Z)) * f_{\rm bin} * f_{\rm IMF}$.

$\mathcal{F}(z', z, Z)$, on the other hand, takes the form

$$\mathcal{F}(z', z, Z) = \frac{\mathcal{N}(z, Z)}{\mathcal{N}_{\rm TOT}(Z)} p(z', Z) \tag{2.3}$$

where $\mathcal{N}(z, Z)$ is the number of CBs that form from stars with metallicity Z and merge at redshift z and $p(z', Z)$ is the distribution of stellar metallicities calculated using the average metallicity evolution from (Madau & Fragos, 2017). This information is then combined with the SFRD, which, for pop I/II, is calculated following once again the prescription by (Madau & Fragos, 2017).

An additional feature of CosmoRate is the possibility to generate a set of catalogues, one for each z bins, each one containing a sample of the objects that merge at that redshift, providing a useful tool to study the statistical properties of the systems at different z.

2.1.1 Customization

In this thesis, Cosmo$\mathcal{R}$ate has been utilized to calculate the MRD in the case of population III stars; in particular, our treatment has been limited to the BBHs that form from isolated binaries. To adequately treat this early stellar population, it was necessary to customize different aspects of the code. Here the main differences from previous implementations are summarized.

Parameter settings

Firstly, the maximum redshift of integration in eq. 2.1 is set to $z_{\max} = 40$, since mergers from pop III event are expected soon after the first star formation, and star formation is expected to be prevented above that redshift (sec. 1.1.1). Secondly, the binary fraction is set to $f_{\rm bin} = 0.69$ following the binary fraction of most massive observable stars (Sana et al., 2012), and the IMF fraction is set to $f_{\rm IMF} = 1$ since we assume to sample the entire pop III IMF using our mass range. For pop III stars those 2 parameters are still unknown, but in the context of MRD calculation we can assume that they are just global scaling fractions and have thus no impact on our model comparison.

Metallicity dependence

One key difference with respect to the previous implementation of Cosmo$\mathcal{R}$ate is that in our work the catalogues of compact binaries are all generated at the same metallicity, as explained and motivated in sec 2.2.1. Removing the metallicity dependence greatly simplifies the calculation of the MRD, that now assumes the form

$$\mathcal{R}(z) = \frac{d}{dt_{\rm lb}(z)} \int_{z_{\max}}^{z} \psi(z') \frac{dt_{\rm lb}(z')}{dz'} \eta \mathcal{F}(z) dz' \; Gpc^{-3} yr^{-1}, \tag{2.4}$$

where $\eta = \mathcal{N}_{\rm TOT}/M_{\rm TOT}$ and $\mathcal{F}(z) = \mathcal{N}(z)/\mathcal{N}_{\rm TOT}$.

Pop III SFRD prescriptions

Lastly, the most important deviation from the original implementation is the prescription of the SFRD. While for pop I/II stars, the SFRD has been derived with observations, the SFRD for pop III stars is still out of reach for observers, and its prescriptions have thus to rely on theoretical models. In my thesis, I have considered several different pop III SFRD models, since the debate on this topic still fails to converge to a unanimous results.

The main characteristics of each considered SFRD model are presented and visually compared in fig 2.1.

De Souza et al. (2011) present a semi-analytical model to derive the SFRD of pop III stars. It takes into account three effects: (1) the effect of the radiative feedback on pop III star formation, mainly the Lyman-Werner flux - following (Greif & Bromm, 2006) - (2)the inhomogeneous reionization of the intergalactic

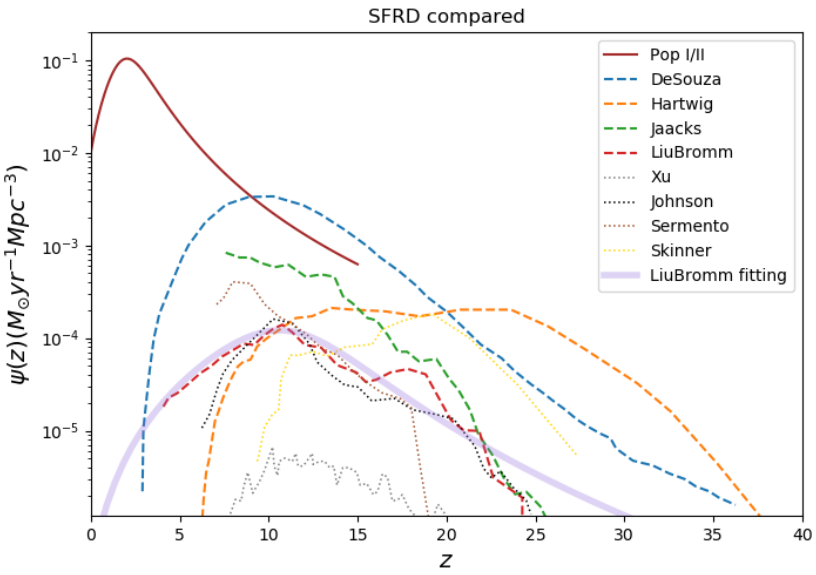

Figure 2.1: Comparison between the pop III different star formation rate density prescriptions. Source model from (de Souza et al., 2011) in blue, (Hartwig, Volonteri, et al., 2016) in orange, (Jaacks et al., 2019) in green and (Liu & Bromm, 2020a) in red with its fitting formula in purple. The thin dotted lines represent the SFRD from (Johnson et al., 2013) black and (Sarmento et al., 2018) brown - both not included on our implementation for the close similarity with (Liu & Bromm, 2020a) - (Xu et al., 2016) grey - to be regarded more as a lower limit since it focuses on very low-density regions - (Skinner & Wise, 2020) yellow, non representative due to the small box size of their simulation. For a further comparison, pop I/III SFRD from (Madau & Fragos, 2017) is also present in the plot in brick-red.

medium - following (Wyithe & Loeb, 2003) -, and (3)the chemical evolution (metal enrichment) of the IGM, following (Johnson, 2010).

Pop III stars in this model are divided into two sub-populations, treated separately: (1) the very first stars born from the primordial gas, referred as pop III.1. Those stars have typical mass $M_{\mathrm{popIII,1}} \sim 1000$ M$_\odot$ (Tegmark et al., 1997). (2) The metal free stars that are born in an environment already influenced by the feedback of pop III.1 stars, e.g the UV radiations - as seen in sec 1.1.1- which are named pop III.2. The hotter and partially ionized medium at the formation epoch lower the typical mass of this second sub-population to $M_{\mathrm{popIII,2}} \sim 40 - 60$ M$_\odot$ (Johnson & Bromm, 2006).

Based on the electron scattering optical depth inferred from the cosmic microwave background, (Inayoshi et al., 2016) find that the SFRD of pop III stars

should be lower by at least a factor of two, with respect to the result of (de Souza et al., 2011). Even with this correction, the pop III SFRD estimated by (de Souza et al., 2011) is the most optimistic calculated in the literature, with a peak value of $\sim 3 \times 10^{-3}$ $M_{\odot}yr^{-1}Mpc^{-3}$ at $z \sim 10$ as can be seen in fig. 2.1 where the sum of the contribution from pop III.1 and pop III.2 are showed. A number of later studies base their calculations on this SFRD prescription (Kinugawa et al., 2014, 2016, 2020, 2021a; Belczynski et al., 2017; Ng, Vitale, Farr, & Rodriguez, 2021; Hijikawa, Tanikawa, Kinugawa, Yoshida, & Umeda, 2021; Kinugawa, Nakamura, & Nakano, 2021b).

Hartwing et al. (2016) A different semi-analytical model to describe the formation of the first stars is carried on by (Hartwig, Volonteri, et al., 2016). In this method, the star forming minihaloes are identified according to a set of criteria - mainly to guarantee H_2 efficient cooling - detailed in (Hartwig, Bromm, Klessen, & Glover, 2015; Hartwig, Latif, et al., 2016). Compared to (de Souza et al., 2011), the resulting SFRD appears (fig 2.1) an order of magnitude lower at its peak ($\sim 2 \times 10^{-4}$ $M_{\odot}yr^{-1}Mpc^{-3}$ at $z \sim 15$). Moreover, later works e.g. (Liu & Bromm, 2021) point out that the criteria chosen for the treatment of cooling are too idealized in this model and consequently tend to overproduce pop III stars at higher redshift $z > 15$.

Jaacks et al. (2019): (Jaacks, Thompson, Finkelstein, & Bromm, 2018) and (Jaacks et al., 2019) reconstruct the star formation history using the hydrodynamical N-body code GIZMO (Hopkins, 2015) coupled with a sub-grid model to assess the legacy of pop III stars (in particular the chemical and radiative feedback in both core-collapse or pair-instability SN scenarios). As shown in fig 2.1, the function found from this simulation rises smoothly from $z = 25$ up to $z = 7$, where it is artificially truncated. The authors nonetheless expect it to go to zero within $z = 6$, hence, in our implementation of the model, the SFRD is set to zero when the information on functional behaviour ends ($z = 7$).

Liu and Bromm (2020): The simulation setup in (Liu & Bromm, 2020a) is very similar to the one adopted by (Jaacks et al., 2018, 2019) with an additional prescription for the thermal (heating) and the mechanical (SN-driven wind) feedback from SN explosions. These prescriptions result in a stronger suppression of pop III star formation with respect to (Jaacks et al., 2019), visible in the progressive departure of the two functions in fig 2.1. This model returns the most pessimistic SFRD among the ones we implemented in cosmo$\mathcal{R}$ate (in $z \sim 10 - 20$). Another peculiarity of this paper is that the authors extrapolate a fitting formula for pop III SFRD adopting the functional form of the pop I/II SFRD from (Madau & Fragos, 2017). The resulting fitting formula reads:

$$\psi(z) = \frac{765.7(1+z)^{-5.9}}{1 + [(1+z)/12.8]^{-8.5}} \; M_{\odot}yr^{-1}Mpc^{-3} \tag{2.5}$$

This function peaks at $z \sim 11$ where $\psi \sim 10^4$ $M_\odot yr^{-1}Mpc^{-3}$

Several more SFRD can be found in literature, e.g. (Johnson et al., 2013; Xu et al., 2016; Sarmento et al., 2018; Skinner & Wise, 2020), nonetheless, the four SFRD we decided to implement provide a representative sample of the possible expectation it is reasonable to have on this function.

2.2 SEVN

The input catalogues that Cosmo$\mathcal{R}$ate uses to derive information on stellar evolution of the systems are generated by the state-of-the-art population synthesis code SEVN, developed by (Spera et al., 2019).

This code is capable of simulating both the single stellar evolution and the binary interactions between the components. Unlike most population syntheses codes, SEVN implements stellar evolution via interpolation over a grid of stellar evolution tracks (instead of polynomial fitting formulas, as originally done by (Hurley, Pols, & Tout, 2000)). These evolutionary tracks, derived from PARSEC (Bressan et al., 2012; Chen et al., 2015), contain information on star and core mass, star and core radius, stellar metallicity and evolutionary stages, covering a vast range of ZAMS masses and metallicities $Z_{\rm ZAMS} \in [10^{-4}, 6 \times 10^{-2}]$, $M_{\rm ZAMS} \in [2, 600]$ $M_\odot$.

Alongside this interpolation method, SEVN comprises a set of prescriptions to evaluate SN explosions and binary interactions. To model the outcome of a core-collapse SN, SEVN provides the possibility to choose between five different prescriptions (details in Appendix B of (Spera et al., 2019)). The rapid core-collapse model (Fryer et al., 2012) has been adopted for this thesis. A SN kicks prescription, following (Hobbs et al., 2005; Fryer et al., 2012) is also included in the simulation.

Binary evolution is implemented in SEVN relying on the work of (Hurley et al., 2002). The prescriptions include mass transfer, common envelope (Hurley et al., 2002), tides (Hut, 1981) and decay by gravitational wave emission (P. C. Peters, 1964). We described these processes in sec. 1.1.2, while more details on the prescriptions can be found in (Spera et al., 2019).

It is worth noting that SEVN includes a set of tracks for bare helium cores to follow the evolution of the stars that lose the whole hydrogen envelope after a common-envelope phase.

2.2.1 Customization

For our work, we decided to describe the evolution of pop III stars with the evolutionary tracks SEVN already uses for stars with $Z = 10^{-4}$.

We are aware that this is a higher metallicity with respect to pop III stars (which have $Z \leq 10^{-8}$, (Schneider, Omukai, Inoue, & Ferrara, 2006)). Tracks with a lower metallicity will be used in our version of the code as soon as the

corresponding stellar-evolution tables are produced[1].

The decision to use $Z = 10^{-4}$ may have introduced some bias in our results. As we introduce in sec 1.1.2 as a consequence of delayed ignition of the CNO cycle in metal free stars with mass with masses $\gtrsim$ 20 $M_\odot$, we expect the typical radius of this population to be relatively small compared to their masses (Ohkubo et al., 2009; Windhorst et al., 2018). The model we use fails to reproduce this result, producing a population of object with larger size. One possible consequence is an overproduction of binary interaction, especially in close binaries. Nonetheless more studies are needed in order to asses whether this assumption carries any significant bias to the results.

The most impacting characteristic of metal free stars, with regards to our investigation, is their suppressed stellar mass loss that allows for the efficient creation of massive BHs. In fig. 2.2 we plotted the the initial and the remnant mass in the range in the mass range (10−300 $M_\odot$) alongside the masses evolution from stars with 20, 50, 80, 200, 250 $M_\odot$ generated with SEVN using $Z_{\rm ZAMS} = 10^{-4}$. The plots show how already at $Z_{\rm ZAMS} = 10^{-4}$ the the mass loss is heavily suppressed and most of the stellar mass in conserved throughout the evolution. For this reason we deem justifiable to simulate the evolution of pop III star using this setup.

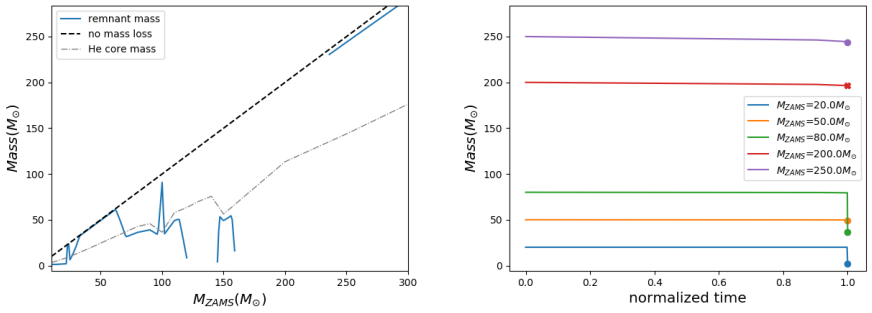

Figure 2.2: Left: the Comparison between $M_{\rm ZAMS}$ of a star and the remnant it produces according to the evolutionary tracks and the SN prescription we used for our simulation. Right: the mass evolution for star that experience different final fates with the lifetime normalized to 1. It appears clear that the only single stellar evolution process capable of significantly modify the mass of the object is its SN mechanism. When the plot end with an X, the star left no remnant.

An aspect of the simulation we do modify is the distribution of initial conditions from which the simulations start. Each binary system begins its evolution with a set of initial conditions (such has metallicity, components masses, semi major axes and eccentricity) assigned according to a chosen probability distribution function. To assess the distribution functions of pop III initial conditions

[1]The generation of the very metal-poor tracks is currently ongoing and requires some important changes to the treatment of stellar winds and opacity in the code.

we must take into account the extremely peculiar environment in which they formed, and consequently the possibility that these distribution functions can be very different from the one observationally constrained for later population stars.

As we just argued, all the simulations are carried on using the lowest metallicity available for SEVN ($Z_{\rm ZAMS} = 10^{-4}$).

Pop III binary initial condition prescriptions

As for the cosmic SFRD of pop III stars, several different prescriptions from preexisting works have been taken into consideration to account for the vast range of possible models proposed in literature. In the following, we summarize the models we considered in this thesis.

Initial Mass Function

As introduced in sec 1.1.1, a consequence of the slower H_2 cooling and of the more effective accretion mechanism with respect to later population stars is that the mass spectrum of pop III is expected to be shifted toward more massive objects. In particular, the initial mass function - the distribution of masses with which stars are formed - for pop III stars is expected to be top-heavy - i.e. that favours formation of high mass stars - (Bromm, Coppi, & Larson, 1999; Bromm & Larson, 2004), as opposed to the top-light IMF suggested by observational constraints on pop I/II stars. The IMF is described by a power law

$$f(M) \propto M^{\alpha} \tag{2.6}$$

plus, in some cases, an exponential cut. The models implemented differ in the slope α of the function and in the presence or absence of the cut.

$\alpha = -2.35$: Salpeter IMF. The present day IMF of stars in the solar neighborhood can be approximated by a simple declining power law for masses above ~ 0.5 $M_\odot$, as constrained by multiple works since (Salpeter, 1955). We decided to included this top-light IMF in the model comparison since it has been considered to extrapolate the mass distribution for pop III stars in a number of studies, e.g. (de Souza et al., 2011; Kinugawa et al., 2014; Johnson et al., 2013; Inayoshi et al., 2016; Xu et al., 2016). Following (Larson, 1999), it is possible to include the tendency of early stars toward higher masses by introducing an exponential mass cut to truncate the lower end of the distribution. The mass scale for the cut is expected to be related to the typical Jeans mass of protostellar clouds. Following (Valiante, Schneider, Volonteri, & Omukai, 2016), we can write $f(M) = M^{-2.35}\exp(-M_{\rm cut}/M)$ with $M_{\rm cut} = 20$ $M_\odot$.

$\alpha = -1$: log-flat IMF. Studies of pop III star formation history by means of cosmological hydrodynamics simulations - e.g. (Susa et al., 2014; Hirano et al., 2014; Hirano, Hosokawa, Yoshida, Omukai, & Yorke, 2015) - conclude that

the IMF of pop III stars is consistent with a flat distribution in logarithmic mass space. Such an assumption has then been adopted by several successive investigations (Sarmento et al., 2018; Tanikawa et al., 2020; Liu et al., 2021; Hijikawa et al., 2021; Tanikawa, Chiaki, et al., 2022; Tanikawa, Yoshida, et al., 2022).

$\alpha = -0.17$: near-flat IMF. Other hydrodynamics simulations return an even stronger preference toward the high mass stars, up to reach an almost flat (Greif et al., 2012; Stacy & Bromm, 2013; Kinugawa et al., 2016) - or, in some cases, completely flat (Kinugawa et al., 2014; Hartwig, Volonteri, et al., 2016; Inayoshi et al., 2016; Kinugawa et al., 2016, 2020) - IMF. Moreover, also in this case it is possible to truncate the distribution for low mass stars by introducing an exponential cut (Jaacks et al., 2018, 2019; Liu & Bromm, 2020a), so that $f(M) = M^{-0.17}\exp(-M_{\rm cut}^2/M^2)$ with $M_{\rm cut}^2 = 20$ $\mathrm{M}_\odot^2$

In all the considered cases, we sampled the stars in the mass range $M \in [10, 300]$ $\mathrm{M}_\odot$ similarly to (Inayoshi et al., 2016; Hartwig, Volonteri, et al., 2016; Skinner & Wise, 2020; Tanikawa et al., 2020). This range allows to explore a wide interval of BH masses, even above the pair instability mass gap (detail in sec. 1.1.3) and limit the influence of the exponential mass cut, as shown in fig. 2.3. Higher $M_{\rm max}$ - in the order of 10^3 $\mathrm{M}_\odot$ - originally adopted by e.g.

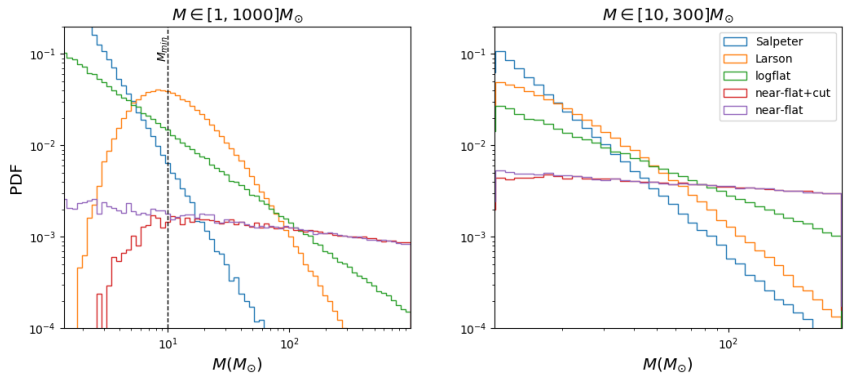

Figure 2.3: The IMF generated using different mass range: $M_{\rm ZAMS} \in [1, 1000]$ left, $M_{\rm ZAMS} \in [10, 300]$ right. The lower mass cut have a significant impact on the mass distribution only at lower mass than $M_{\rm min}$. In particular the near-flat IMF ($\alpha = -0.17$, in red and purple) is unaffected by the presence of a lower mass cut for our choice of mass range. For this reason only one of these two models (the one from (Liu & Bromm, 2020a), in red) will be taken into account and referred as near-flat henceforth.

(Abel et al., 2000; Abel, Bryan, & Norman, 2002; Hirano et al., 2014) are now ruled out by state of the art fragmentation model (Greif et al., 2012; Susa et al., 2014). On the other hand, $M_{\rm min}$ lower than ~ 10 $\mathrm{M}_\odot$ - up to 0.1, as suggested

in the work of (Stacy & Bromm, 2014) - are deemed unlikely by recent works on chemical abundance pattern in carbon enriched extremely metal poor stars (Tanikawa, Chiaki, et al., 2022). The debate on the typical mass range expected for pop III is nonetheless still open.

Mass ratios

In a binary we define q as the ratio between the masses of the components M_2/M_1, with $M_2 \leq M_1$ by definition, so that $q \in [0.1, 1]$. As introduced in sec. 1.1.1 the treatment of the interplay between accretion and fragmentation can drastically change the final picture. We implement four different prescriptions representative of the possible functional behaviour (fig 2.4). In most cases the distribution appear as a power law

$$f(q) \propto q^{\beta} \tag{2.7}$$

$\beta = -0.1$: Sana et al. (2012) (Sana et al., 2012) analyze a large sample of nearby massive O stars - 71 objects (of which 40 binaries)- and measure all their relevant properties. The intrinsic statistical distributions of mass ratios, orbital periods and eccentricities is then uncovered using a Monte Carlo approach to identify, and thereby subtract, the observational biases. Prescriptions for pop III binary statistic based on this paper can be found e.g. in (Inayoshi et al., 2016; Tanikawa, Chiaki, et al., 2022; Tanikawa, Yoshida, et al., 2022). For the mass ratio in particular, the distribution found is almost flat. For our work, we implemented a modified version of this probability distribution similarly to (Kinugawa et al., 2020, 2021b; Tanikawa, Susa, Yoshida, Trani, & Kinugawa, 2021; Hijikawa et al., 2021): once the secondary mass is sorted according to $f(q)$ it is checked if it lies outside the initial mass range chosen (that is if $M < M_{\rm min} = 10$ M$_\odot$). If this is the case, the mass is sorted again from the same distribution. The process is repeated until the mass sorted meets the requirement $M > M_{\rm min}$. The consequence of this additional requirement is that the resulting probability distribution depends on the IMF chosen: since $M_2 \leq M_1$ and $M_2 > M_{\rm min}$, when the IMF favours primary stars with mass close to $M_{\rm min}$, q will be more peaked toward higher q (similar masses) while top-heavy IMF will led more flat q distribution, see fig. 2.4.

$\beta = 0$: Random coupling : This model randomly couple by two the masses sorted from the chosen IMF, returning a flat distribution of q. For each binary, the star with the higher mass will be taken as the the primary and its lower mass companion as the secondary. This prescription is used e.g. by (Kinugawa et al., 2014; Inayoshi et al., 2016; Kinugawa et al., 2020; Liu et al., 2021; Tanikawa, Chiaki, et al., 2022).

Sorted-coupled : We also implemented a model that favours the formation of systems with similar mass stars, as suggested by (Pinsonneault & Stanek, 2006; Oh, Kroupa, & Pflamm-Altenburg, 2015). In this model, all the stars are

generated according to the initial mass function, then randomly divided in group of 10 - to simulate a minihalo environment - and finally sorted and coupled by mass similarity, so that the more massive forms a binary with the second more massive and so on. Similar prescription is used e.g. in (Hartwig, Volonteri, et al., 2016; Tanikawa, Chiaki, et al., 2022).

$\beta = -0.55$: Stacy & Bromm (2013) (Stacy & Bromm, 2013) models the formation and evolution of pop III systems in a range of host minihalo environments via a cosmological simulation. This simulation predicts a tendency toward the formation of a massive star in the center of the protostellar cloud with a smaller secondary companion. As consequences of that, the mass ratio distribution they find is packed toward lower value of q ($q = 0.1$). Later studies e.g. (Belczynski et al., 2017; Jaacks et al., 2019) adopt this model to assess the binary initial conditions.

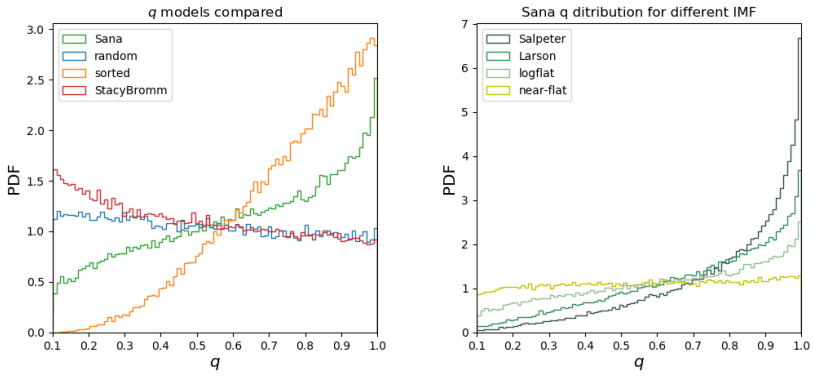

Figure 2.4: Left: the different probability density function compared. Modified version of (Sana et al., 2012) in green, random model in blue, sorted-coupled model in orange, Stacy & Bromm model (Stacy & Bromm, 2013) in red. All these distributions are generated starting from a log-flat IMF. Right: How the modified version of (Sana et al., 2012) model changes for different IMFs.

Orbital period

The semi major axes - and consequently the orbital periods - are extremely important to determine the nature of the binary interaction within a system and the in-spiral timescale due to GW emission decay, as described in sec 1.1.2. In our work, we implemented three models for the probability distribution function of the orbital period, each one characterized a cumulative distribution function with the form

$$F(P) \propto \log(P)^{\gamma} \tag{2.8}$$

$\gamma = 0.45$: Short period The prescription from (Sana et al., 2012) finds a strong preference for close binaries. The distribution peaks at $P \sim 10^0$ *days* which correspond to $a \sim 10^1$ $R_\odot$ and is sampled in a the range $log(P) \in [0.15, 5.5]$, with P in days, following (de Mink & Belczynski, 2015). This prescription is consistent with the one used in e.g. (Hartwig, Volonteri, et al., 2016)

$\gamma = 2.54$: Long periods The simulation from (Stacy & Bromm, 2013), on the other hand predicts a more spread distribution, peaked at longer periods with respect to (Sana et al., 2012). Following the interpolation on the cumulative distribution reported in (Stacy & Bromm, 2013), the resulting period distribution packs at $\sim 10^3$ days ($a \sim 10^4$ $R_\odot$). The range of periods from with the distribution is sampled was set to $log(P) \in [0, 4]$, with P in years.

Intermediate periods We additionally implement an intermediate prescription, that use the same slope as the long period prescription ($\gamma = 2.54$) and the same sampling range as the small period prescription $log(P) \in [0.15, 5.5]$, with P in days. The distribution obtained in this way peaks at $\sim 10^1$ days ($a \sim 10^2$ $R_\odot$) and present an higher number of large binaries ($a \gtrsim 10^3$ $R_\odot$) with respect to the prescription from (Sana et al., 2012).

All our prescription are roughly consistent with a log-flat distribution of semi major axis (sampled in different ranges) as proposed by (Abt, 1983) and adopted by (Kinugawa et al., 2016), (Kinugawa et al., 2020), (Hijikawa et al., 2021). In fig 2.5 we show this behaviour.

It is interesting to cite the model decision carried on by (Belczynski et al., 2017) which simulate two distinct populations, one with short orbital period (Greif et al., 2012) and one with long orbital period (Stacy & Bromm, 2013), summing their effect afterward. This model, however, has not been implemented in out work.

Eccentricity

The last initial condition distribution we take into account is the initial distribution of eccentricity. Despite the fact that eccentricity can experience heavy modification throughout the system evolution, its initial distribution can impact the evolution of the systems favouring binary interaction triggered by component close encounter at the periastron. Two models for the initial eccentricity have been implement for our work - and displayed in fig. 2.5 -, both with the functional form

$$f(e) \propto e^{\delta} \tag{2.9}$$

$\delta = 0.42$: Sana (2012) Using once again the results obtained by (Sana et al., 2012), the initial eccentricity distribution have a clear preference toward circular orbits.

$\delta = 1$: thermal eccentricity A common choice for the distribution of eccentricity for pop III binaries follows (Heggie, 1975), which favours eccentric systems. This prescription is adopted e.g. by (Kinugawa et al., 2014; Hartwig, Volonteri, et al., 2016; Liu et al., 2021; Tanikawa, Chiaki, et al., 2022). We couple this eccentricity distribution to the long (and Intermediate) period prescription since this distribution is expected from population that are affected by dynamical interaction and large binaries ($a \gtrsim 10^3$ R$_\odot$) rend to be more affected by those interactions (Duquennoy & Mayor, 1991).

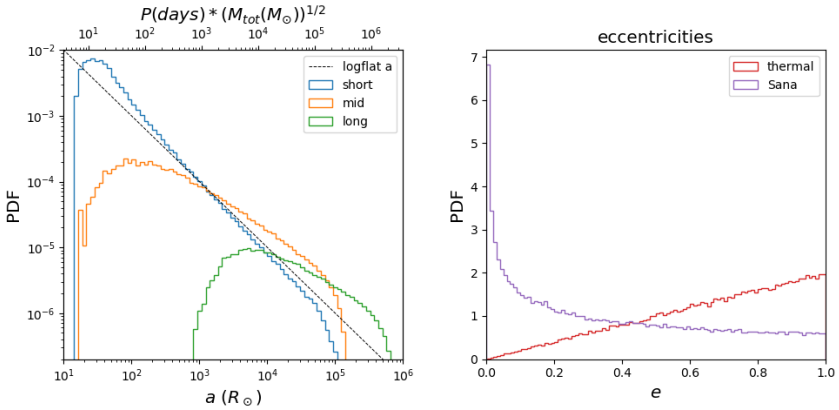

Figure 2.5: Left: the three possible prescriptions for the period compared, the first has a peak at $a \sim 10^1$ R$_\odot$ while the second has a peak as $a \sim 10^2$ R$_\odot$, the third at $a \sim 10^4$ R$_\odot$ the dashed black line is $\propto a^{-1}$. Right: prescriptions for the initial eccentricity distribution compared.

Chapter 3

Results

3.1 Simulation runs

3.1.1 Input catalogues

In order to obtain the input catalogues, we used SEVN to generate 16 starting catalogues of binary compact objects with different simulation setup. For each different simulation setup, - characterized by a set of prescriptions to describe the distribution of the initial conditions -, SEVN simulated the evolution of 10^7 binaries, from which we then selected only the systems that reached coalescence in an Hubble time ($t_{\rm del} < 14$ Gyr) to compose the input catalogue. In tab. 3.1 we present a summary of the possible prescriptions implemented while in tab. 3.2 we report the setup of each input catalogues generated with SEVN we used in our model comparison.

In the present section we compare the different input catalogues obtained and investigate the impact that different initial conditions distribution have on merger efficiency, delay time and chirp mass distribution.

Merger efficiency

In table 3.3 we report the total simulated mass of each starting catalogue, the number of systems that merge within an Hubble time and the merger efficiency η calculated as $\eta = (\mathcal{N}_{\rm tot}/M_{\rm TOT,sim}) \times f_{\rm bin} \times f_{\rm IMF}$ where $f_{\rm bin} = 0.69$ and $f_{\rm IMF} = 1$. The choice of $f_{\rm IMF} = 1$ relies on the simplified assumption that we are sampling from the entire pop III mass range, whereas we set $f_{\rm bin} = 0.69$ following the local binary fraction for O-type stars with $M > 15$ M$_\odot$, observed by (Sana et al., 2012).

For pop III stars, η is taken as a constant for each input catalogue as opposed to pop I/II stars. In this latter case, indeed, the merger efficiency is dependent on metallicity i.e. it increases with decreasing metallicity, due to the higher BH masses and easier CE development/survival at low $Z_{\rm ZAMS}$ (Belczynski, Dominik, et al., 2010). Moreover, the values of η found for pop III binaries are often

Scheme of all the models implemented							
IMF $M \in [10, 300]$ $M_\odot$		q (M_2/M_1) q$\in [0.1, 1]$		orbital period [a]		eccentricity $e \in [0, 1]$	
Name	$f(M) \propto$	Name	$f(q) \propto$	Name	$F(P) \propto$	Name	$f(e) \propto$
Salpeter	$M^{-2.35}$	Sana	$q^{-0.1}$ [b]	short	$\log(P)^{0.45}$	Sana	$e^{-0.42}$
Larson	$M^{-2.35}e^{-(\frac{M_{\rm cut}}{M})}$ [c]	random	cost	mid	$\log(P)^{2.54}$	thermal	e
logflat	M^{-1}	sorted	[d]	long	$\log(P)^{2.54}$		
near-flat	$M^{-0.17}e^{-(\frac{M^2_{\rm cut}}{M^2})}$ [e]	StacyBromm	$q^{-0.55}$				

[a] Short and intermediate assume a cumulative distribution of periods in days inside the range $log(P(days)) \in [0.15, 5.5]$. Long period distribution assumes a cumulative distribution of periods in years inside the range $log(P(yr)) \in [0, 4]$ yr.

[b] If $M_2 < 10$ $M_\odot$, the second mass is sorted again from the same distribution. This modification of the original model led to a deviation from the function by Sana, especially with IMF that favour low mass stars.

[c] $M_{\rm cut} = 20$ $M_\odot$ according to (Valiante et al., 2016).

[d] In this model all the stars are generated according to the initial mass function, then randomly divided in group of 10 (to simulate a minihalo environment) and, finally, sorted and coupled by mass similarity (so that the more massive forms a binary with the second more massive and so on).

[e] $M^2_{\rm cut} = 20$ $M^2_\odot$ according to (Liu & Bromm, 2020a).

Table 3.1: Summary table of all the model prescriptions taken into consideration for initial the distribution of primary mass, mass ratio, orbital period, and eccentricity.

Input catalogues				
Cat.	IMF	q	P	e
Sa_1	Salpeter	Sana	short	Sana
Sa_2	Salpeter	random	short	Sana
Sa_3	Salpeter	StacyBromm	mid	thermal
Sa_4	Salpeter	StacyBromm	long	thermal
La_1	Larson	Sana	short	Sana
La_2	Larson	random	short	Sana
La_3	Larson	StacyBromm	mid	thermal
La_4	Larson	StacyBromm	long	thermal
log_1	logflat	Sana	short	Sana
log_2	logflat	random	short	Sana
log_3	logflat	StacyBromm	mid	thermal
log_4	logflat	StacyBromm	long	thermal
fl_1	near-flat	Sana	short	Sana
fl_2	near-flat	random	short	Sana
fl_3	near-flat	StacyBromm	mid	thermal
fl_4	near-flat	StacyBromm	long	thermal

Table 3.2: Summary of the initial condition distributions setup for each input catalogue considered for our model comparison.

slightly higher than the typical merger efficiency from pop I/II systems due to the abundance of massive stars, which are capable of efficiently generating a BH at the end of their evolution. The last row of the tab 3.3 refers to the merger efficiency of systems at $Z = 0.0001$ from a simulated catalogue of pop I/II binaries generated using SEVN. For all the catalogues - pop III and pop I/II - we found values of η on the same order of magnitude (10^{-5} $M_{\odot}^{-1}$). The catalogues that assume long period distribution exhibit value of η comparable or even lower than pop I/II stars peak value. For those catalogues the effect of the abundance of massive stars is compensated by the typically large size of the systems, that suppresses the possibility of interaction between the component of the binary.

Results of population synthesis simulations			
Cat.	$M_{TOT,sim}$($M_{\odot}$)	$\mathcal{N}_{\rm tot}$	η($M_{\odot}^{-1}$)
Sa_1	470008805	29371	4.31×10^{-5}
Sa_2	561119284	13445	1.65×10^{-5}
Sa_3	424286229	26098	4.24×10^{-5}
Sa_4	423927606	8754	1.42×10^{-5}
La_1	665149041	50606	5.25×10^{-5}
La_2	821421715	31861	2.68×10^{-5}
La_3	620698269	46731	5.19×10^{-5}
La_4	621081886	15673	1.74×10^{-5}
log_1	1330726774	82676	4.29×10^{-5}
log_2	1705846178	64216	2.60×10^{-5}
log_3	1289717751	70883	3.79×10^{-5}
log_4	1289152489	22483	1.20×10^{-5}
fl_1	2239376501	99782	3.07×10^{-5}
fl_2	2907066875	79881	1.90×10^{-5}
fl_3	2197915721	75683	2.38×10^{-5}
fl_4	2197411455	23477	0.74×10^{-5}
$10^{-3}Z_{\odot}$	21571785	1908	1.01×10^{-5}

Table 3.3: Total simulated mass, number of binaries that merge within an Hubble time and merger efficiency of all the different input catalogues generated by SEVN. For pop III catalogues η has been adjusted for the binary fraction $f_{\rm bin} = 0.69$, and assuming $f_{\rm IMF} = 1$. In the last raw we report the merger efficiency at Z=0.0001 for a catalogues of pop I/II stars. For this catalogues we assumed $f_{\rm bin} = 0.4$, and assuming $f_{\rm IMF} = 0.285$.

Confronting $\mathcal{N}_{\rm tot}$ in tab. 3.3 and the number of systems simulated (10^7) we can notice how just a small minority of the simulated systems (less than 1%) met the required condition $t_{\rm del} < 14$ Gyr. The possibility for a system to meet this condition is largely determined by its evolutionary path: only few and peculiar evolutionary channels allow the binary to reach coalescence within an Hubble time. Indeed, a system needs to be in the "favorable conditions" that allow for efficient binary interaction - stable mass transfer or common envelope, which

can significantly modify the orbit - and that provide the possibility to survive the interaction to generate a compact object binary. If the interaction does not take place, the binary is able to survive for a time longer than an Hubble time. If, on the other hand, the interaction is too violent or unstable, the components can merge into a single object before becoming BHs or can split, destroying the binary. It is thus important to investigate the evolutionary channels followed by the systems in our input catalogues and how the initial properties of the binaries can favour or suppress their occurrence. In tab, 3.4 we report the statistical recurrence of each evolutionary channel for the different input catalogues. The majority of the binaries across the input catalogues experience one

Evolutionary channel recurrence										
Cat.	No-CE (%)	$< t_{\rm del}(Gyr) >$	P-CE (%)	$< t_{\rm del}(Gyr) >$	S-CE (%)	$< t_{\rm del}(Gyr) >$	D-CE (%)	$< t_{\rm del}(Gyr) >$	2-CE (%)	$< t_{\rm del}(Gyr) >$
Sa_1	3.3	3.425	0.3	9.469	54.7	1.097	37.6	0.44	4.1	0.255
Sa_2	9.5	3.608	1.2	8.451	65.5	1.241	18.2	0.302	5.5	0.38
Sa_3	1.2	2.218	0.8	9.778	29.2	1.848	63.1	0.283	5.7	0.35
Sa_4	0.8	2.022	0.9	8.965	21.1	2.279	68.9	0.301	8.3	0.45
La_1	2.7	3.371	0.3	10.058	49.5	0.986	43.1	0.471	4.4	0.331
La_2	6.0	3.453	1.2	8.868	60.0	1.017	26.8	0.38	5.9	0.369
La_3	1.0	2.289	0.9	10.294	24.9	1.737	66.8	0.305	6.5	0.347
La_4	0.7	1.992	0.9	9.122	16.8	2.28	71.7	0.349	9.9	0.358
log_1	1.3	3.249	0.3	10.382	46.6	0.621	42.7	0.634	9.1	0.39
log_2	1.4	3.648	0.7	9.634	53.0	0.5	31.9	0.663	13.0	0.404
log_3	0.6	2.466	1.0	10.177	20.3	1.17	63.5	0.477	14.7	0.363
log_4	0.4	1.893	1.2	9.873	8.4	2.289	68.8	0.491	21.1	0.382
fl_1	0.6	3.226	0.3	10.788	46.9	0.441	37.2	0.776	15.0	0.422
fl_2	0.2	3.33	0.3	10.477	48.0	0.351	28.4	0.971	23.2	0.434
fl_3	0.3	2.303	1.0	10.551	19.0	0.798	55.7	0.626	24.0	0.36
fl_4	0.2	1.591	1.2	9.837	4.1	2.226	61.4	0.661	33.1	0.375

Table 3.4: For each input catalogue, the fraction of binaries that experience no common envelope (No-CE), one common envelope phase with only the primary in the giant branch (P-CE), one common envelope phase with the secondary in the giant branch and the primary already a compact remnants (S-CE), one common envelope phase where both of the components are in the giant branch (D-CE) or two CE phases during their evolution (2-CE). Along with those information, we report the mean delay time calculated for each evolutionary channel.

common envelope phase. In particular, for catalogues that favour close binaries and low eccentricity, the common envelope phase takes place mainly when the primary star has already ended its evolution and has become a BH (S-CE). For catalogues that favour large and eccentric binaries, instead, the CE phase is more likely to result in the ejection of both the envelopes and, consequently, the creation of a naked cores binary (D-CE). Looking at the different primary mass distributions it is possible to conclude that a flatter IMF - i.e. that favours higher mass components - increases the probability for the systems to experience two separate CE phases (2-CE) while a steeper IMF[1] leads to an higher fraction of stars that reach coalescence without experiencing a common envelope. The vast majority of the systems that experience a CE phase with the primary in its giant branch and the secondary in main sequence encounter a second CE when, in turns, the secondary become a giant. For this reason P-CE is the least common evolutionary path present in the simulations. It is worth to notice that we found a lower percentage of systems that evolve without experiencing com-

[1]Henceforth, we use the term "steeper IMF" as reference to the Salpeter and the Larson IMF; we use the term "flatter IMF" as reference to the log-flat and the near-flat IMF

mon envelope that previous study, e.g. (Kinugawa et al., 2016, 2020; Inayoshi et al., 2017). The reason for this behaviour can be found in our decision of using the evolutionary track of metal-poor pop I/II stars to simulate metal free pop III stars. The larger radius resulting from this assumption may favours the creation of a CE, especially when the IMF favours the formation of very massive stars - thus stars with very large radii -. This aspect, however, does not have a major impact on the merger efficiency that result consistent with those previous studies. The lowest merger efficiency we fond is for fl_4 ($\eta = 0.74 \times 10^{-5}$ $M_\odot^{-1}$), where, as we saw, high masses and large semi major axis suppress the possibility for the systems to interact. The highest merger efficiency, on the other hand, is found for La_1 ($\eta = 5.25 \times 10^{-5}$ $M_\odot^{-1}$). Larson IMF returns an higher merger efficiency with respect to Saltpeter - which has the same slope but without the lower mass cut - because the presence of the cut ensure the catalogue that uses this IMF the highest number of objects between ~ 20 $M_\odot$ and ~ 50 $M_\odot$, that is a mass range from which BHs are very effectively produced.

Delay time

The distribution of delay times is shown in fig. 3.1. Two features are immediately visible: an irregular behaviour with more than one peak at low $t_{\rm del}$ ($\lesssim 10^8$ yr) and the asymptotic behaviour that roughly matches a $t_{\rm del}^{-1}$ function.

The former behaviour arises from the evolutionary features of the systems. The insurgence of binary interaction, SN kicks and tides, can alter the binary properties, favoring an earlier merger and creating the different peaks of the distribution we see. The different peaks are indeed related to the preferred evolutionary channel for each catalogue.

The asymptotic behaviour, on the other hand, finds its root in the initial distribution of semi major axis and in the physics of gravitational waves emission. The delay time, indeed, is the result of a convolution of the initial semi major axis distribution - that gets modified by stable mass transfer and CE during evolution - and the time-scale for orbital decay, which is due to the emission of gravitational waves once the BBH is formed (Belczynski et al., 2017). Stable mass transfer does not drastically modify the orbital size, while CE leads to a significant contraction but still roughly conserving the shape of the distribution of orbital separations. From (P. C. Peters, 1964), GW decay timescale is $\propto a^4$, while our prescription on a roughly resembles a distribution of semi major axis $\propto a^{-1}$, as we show in fig 2.5. Following (Belczynski et al., 2017) we can see that, for large enough systems ($a \gtrsim 1000$ $R_\odot$) and assuming a log-flat distribution of the semi major axis, the delay time scales like $a^{-1}(da/dt)_{GR} \propto t^{-1/4} d(t^{-1/4})/dt \propto t^{-1}$. This simple approximation justifies the functional behavior visible in fig. 3.1.

Before focusing on the differences between the input catalogues, one important aspect to investigate is the impact of the stable mass transfer on the distribution of $t_{\rm del}$. In figure 3.2 we plotted the distribution of $t_{\rm del}$ from a single catalogue (La_1) dividing the objects that experience at least one common envelope and the objects that reach merger only through stable mass transfer.

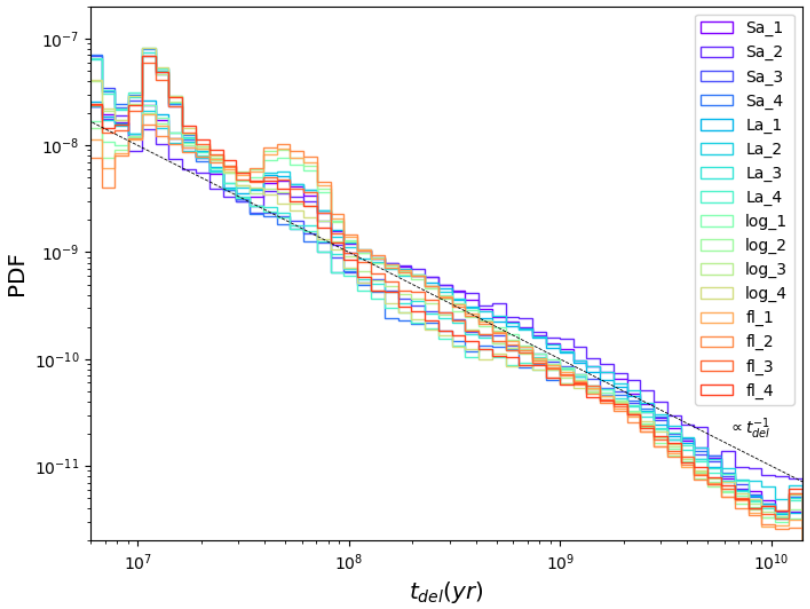

Figure 3.1: $t_{\rm del}$ distribution for all the input catalogues considered. The black dashed line is $\propto t_{\rm del}^{-1}$ and roughly matches the slope of the distribution for $t_{\rm del} \gtrsim 10^8$ yr. For $t_{\rm del} \lesssim 10^8$ yr three distinct peaks are visible: at $\sim 5 \times 10^6$, at $\sim 10^7$ and at $\sim 5 \times 10^7$.

The systems that evolve without CE show a flatter distribution, since their orbit does not shrink efficiently throughout their life. This behaviour can be found in all the catalogues. Moreover, tab. 3.4 shows how different evolutionary channels have very different mean delay times. The mean $t_{\rm del}$ for systems that avoid common envelope during their evolution stands around few Gyr, higher than the value found for systems that went through at least one CE phase. The only exemption to this observation is given by the few systems that evolve through S-CE, and return values of mean $t_{\rm del}$ even higher with respect to the No-CE case, reaching $\sim$ 10 Gyr. As we will see later in this section, however, this behaviour is caused by a selection effect, since a binary needs to be in a very peculiar condition to undergo a CE phase when the secondary is in its main phase and successively avoid a second CE when it enters the giant branch.

The S-CE scenario presents a mean $t_{\rm del}$ around 1 Gy, which is shorter than P-CE and No-CE but still much higher than the evolutionary channel D-CE and 2-CE. Those last two channels, indeed, return the lowest mean $t_{\rm del}$ across the systems simulated.

The short delay time from D-CE can be understood considering a stronger

contraction is necessary to overcome the binding energy of both the envelope together. Finally, a typically short $t_{\rm del}$ is expected from the systems that experience two common envelopes throughout their life (2-CE) since the contraction caused by this phase is reiterated a second time during their evolution.

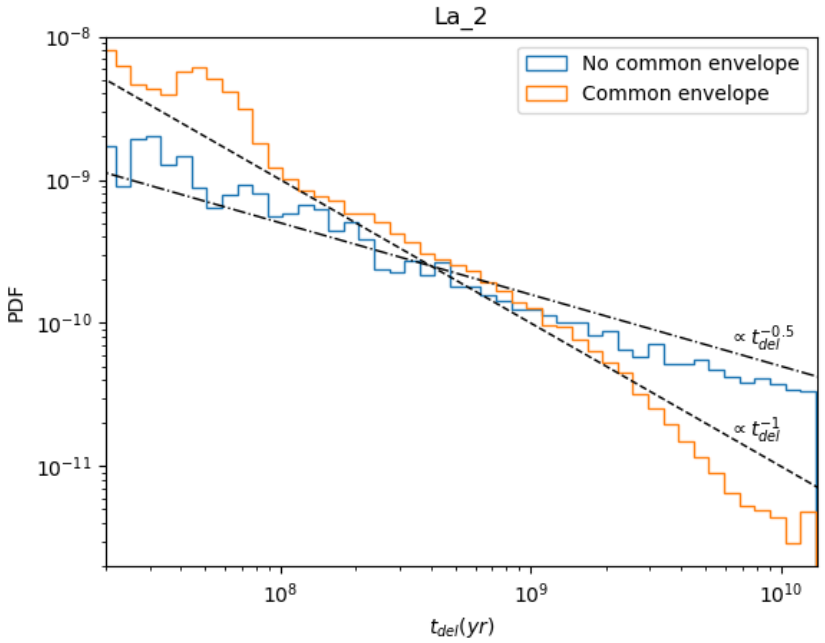

Figure 3.2: $t_{\rm del}$ distribution (of the catalogue La_2) dividing the systems that experience a CE phase from those who do not. The slope of those distributions do not significantly change if computed using a different catalogue.

A further investigation can be carried on by looking at the delay time distribution with respect to the binary initial conditions and evolutionary channels. For this purpose, in fig. 3.3 we plotted a series of 2D histograms that correlate the binary properties with $t_{\rm del}$ and show how each catalogue populates those 2D-spaces differently. In addition to that, fig. 3.4 highlight the crucial role of the evolutionary path in determining the location of the systems inside the histograms. For an easier reading here we only display the plots obtained from 3 catalogues (Sa_1, log_2, fl_3). The analysis, however has been carried on considering the complete set of plots.

The first row reports the total mass distribution with respect to the delay time. Systems with $M_{\rm ZAMS,tot} \gtrsim 60$ M$_\odot$ experience a positive correlation between total mass and $t_{\rm del}$ but they rarely have $t_{\rm del} > 10^8$ yr. As we will see in the next section, this behaviour produces a merger rate density that closely follows the SFRD.

A correlation between the system mass and the evolutionary channel followed is clearly visible. We can distinguish three mass ranges: (1) $\sim 60 - 170$ $M_\odot$, dominated by D-CE, (2) $\sim 170 - 250$ $M_\odot$, dominated by S-CE and finally (3) $\gtrsim 250$ $M_\odot$ where only systems that evolve as 2-CE can be found.

In addition to that, a sub-population of systems emerges in the lower part of the mass spectrum ($M \sim 50$ $M_\odot$). Those objects are more homogeneously distributed along the delay time, reaching value comparable with Hubble time. The evolutionary channels found in this region are S-CE and No-CE. Catalogues that assume a steeper IMF populate this lower region more intensely. This behaviour justifies the higher mean $t_{\rm del}$ found for those catalogues.

Shifting the attention towards mass ratios, the plots clearly show how most of the systems that compose the input catalogues possess a value of q close to 1. Systems with very low mass ratios are very likely to undergo D-CE as the who component have very similar lifetimes and consequently they can reach the giant phase at the same time. A notable exception is a sub-population of high mass ratio systems ($q \sim 0.3 - 0.8$) which merges after $\sim 10^8$ yr, linked to the population of very massive stars ($M_{\rm tot} \gtrsim 170$ $M_\odot$) with evolutionary channels S-CE or 2-CE.

As seen earlier in this section, there is a clear correlation between the orbital size of the compact binary and the delay time, determined by the gravitational wave decay timescale. Nonetheless the distribution of initial semi major axis only loosely show a positive trend with respect to $t_{\rm del}$. The delay time, indeed seems dominated by the modification to the semi major axis by means of evolutionary process. This is especially visible in the case of D-CE which generate a large number of systems with large initial orbital ($a \gtrsim 10^3$ $R_\odot$) that have $t_{\rm del} \sim 10^7 - 10^8$ yr. This behaviour can be found in catalogues that assume intermediate and large prescription of P.

Finally, we can see how the correlation between the delay time and the initial eccentricity is weak, since the binary interaction and the SN kicks can modify the system eccentricity in a very effective way. Those processes are often uncorrelated with initial value of the eccentricity and have a dominant role in determining the evolutionary timescale of the systems. The only exception is the visible trend liked to the catalogues that favour large size binaries. When the eccentricity is high, the orbit of the components at their periastron can allow for a close encounter between them. If at a certain point in time the separation between the components is smaller than the sum of their radios - and at least one of them has already developed a dense core -, SEVN trigger a CE phase, and the orbit is circularized. When the orbital size is very large - long distribution of P - the interaction between the component is suppressed due to the distance between them and this scenario becomes the main formation channel. This is also the reason why most of the system in those catalogues follow a D-CE or 2-CE evolutionary path.

In light of what we saw up to this point, we can conclude this section discussing the different peaks of the $t_{\rm del}$ distribution visible in fig. 3.1 and 3.5.

The peak at lowest $t_{\rm del}$ is created by the catalogue that favours large and eccentric binaries (Sa_4, La_4, log_4) in the mass range $M_{\rm tot} \sim 60 - 100$ $M_\odot$.

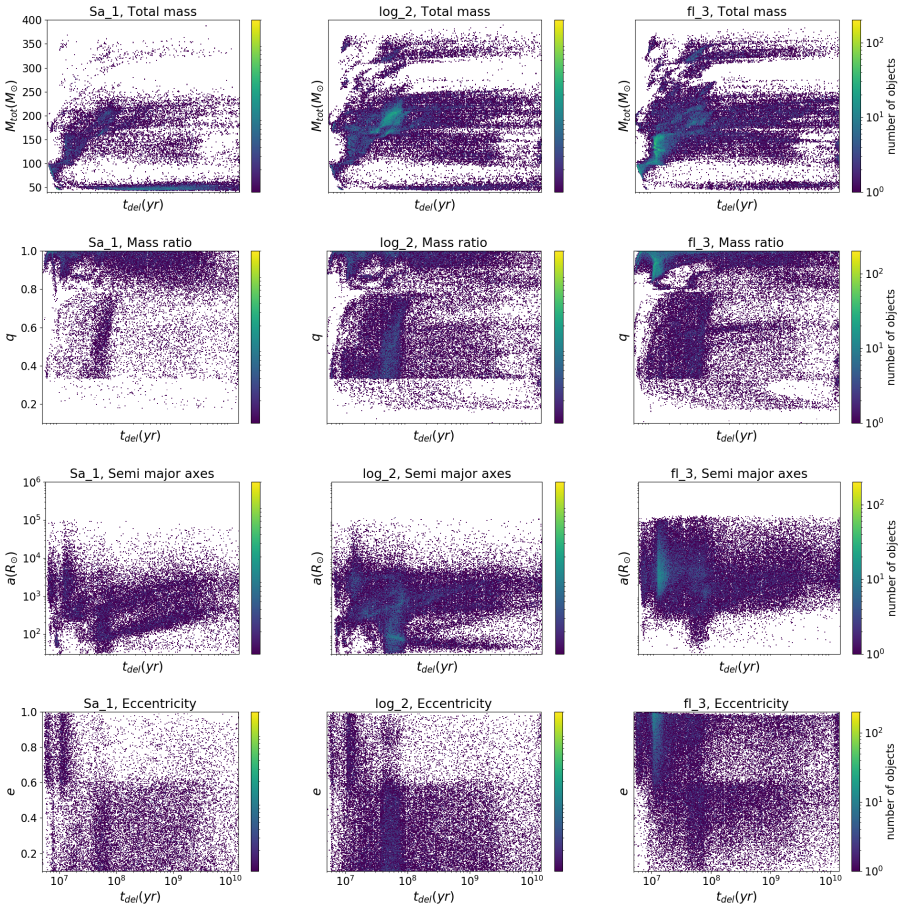

Figure 3.3: The distribution of of binaries in $t_{\rm del}$ with respect to the system initial conditions (total binary mass, mass ratio, semi major axis, eccentricity) for three catalogues: Sa_1 (left column),log_2 (center column),fl_3 (right column). The features are similar for all the catalogues but each of them populate the 2D space of the histograms in a different way depending on their initial condition distribution.

As we saw, the high eccentricity of those systems can cases "close encounters" between the components, that perturb the system equilibrium and shorten its life spam. we does not see the same behaviour for the other catalogues that assume a thermal distribution of e (Sa_3, La_3, log_3, fl_3, fl_4) as the smaller orbital size - or the higher mass - suppress the probability to survive such type of interaction.

The peak of objects with $t_{\rm del} \sim 10^7$ yr can be attributed to the catalogues

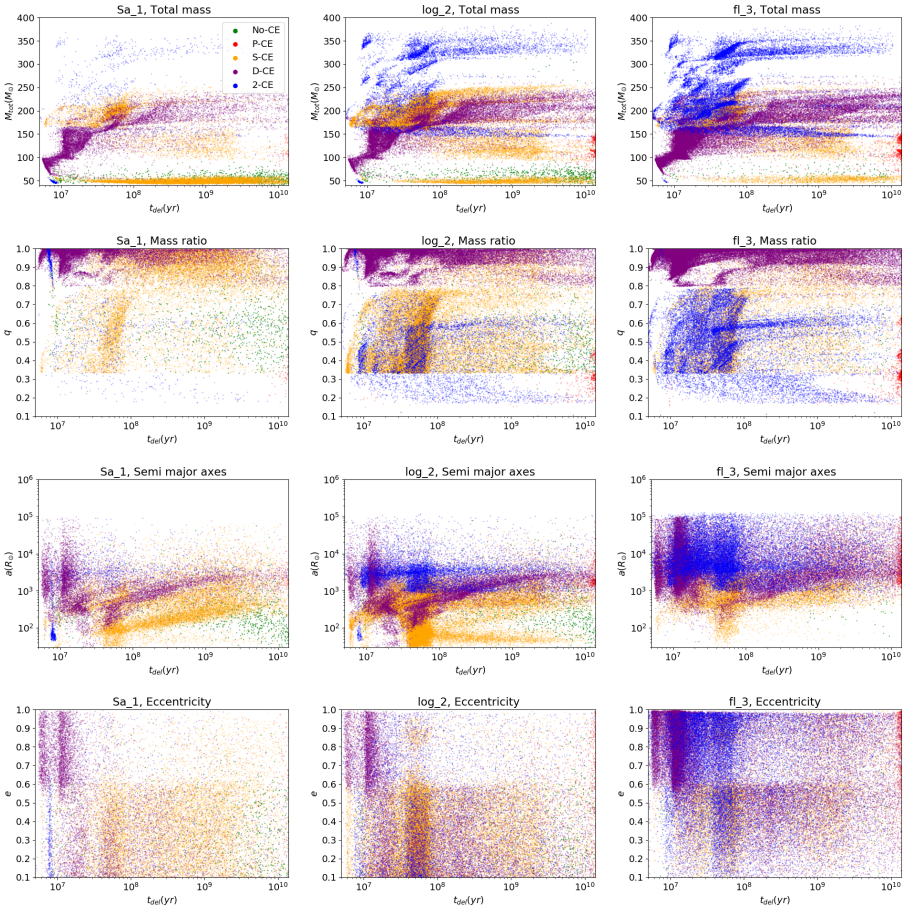

Figure 3.4: The distribution of the evolutionary channel in $t_{\rm del}$ with respect to the system's initial conditions (total binary mass, mass ratio, semi major axis, eccentricity) for three catalogues: Sa_1 (left column),log_2 (center column),fl_3 (right column). Systems that do not experience CE are plotted in green, a single CE with the primary in giant branch in red, with the secondary in giant branch in orange, with both the components giant branch in purple or that experience two CE phases in purple.

(Sa_3, La_3, log_3, fl_3, Sa_4, La_4, log_4, fl_4) and to systems with similar properties to the one constituting the lower peak, but in an higher mass range - $\sim 100 - 170$ $M_\odot$ -. The evolutionary channel D-CE is the main contribution for both those peaks.

For all those catalogues - which have the common feature of assuming the StacyBromm distribution of q - also present a peculiar upward trends in the $t_{\rm del}$

distribution above $\sim 10^{12}$ yr (highlighted in fig. 3.5). The main contributor of this feature is a relatively small population of systems in the mass range $M_{\rm tot} \sim 100 - 170$ M$_\odot$ which shows large orbits ($a \gtrsim 10^3$ R$_\odot$) and very low mass ratios ($q \sim 0.2 - 0.5$). In this peculiar scenario, the primary reaches the giant branch while the much smaller secondary is still in main sequence. When the CE phase is triggered, only the primary envelope contribute to the binding energy, consequently, the contraction needed to eject the envelope and end the CE is much less than , e.g., the D-CE scenario. Since the secondary star has relatively low mass and it is still well separated from the primary remnants, it can continue its evolution without encountering a second CE (i.e. through stable mas transfer of without any interaction), thus efficiently conserving the orbital separation and ending its evolution as a P-CE binary. The $t_{\rm del}$ resulting from this scenario is hence very long and justifies the mean $t_{\rm del}$ we found for the P-CE evolutionary channel in tab 3.4.

The last visible peak in fig. 3.1 can be seen at $t_{\rm del} \sim 10^8$ yr. The the systems responsible for this feature come from the catalogues log_1, fl_1, log_2, fl_2 and, consequently, are mainly very massive ($M_{\rm tot} \sim 170 - 250$ M$_\odot$) with relatively small and orbit ($a \lesssim 10^3$ M$_\odot$). The majority of those systems evolve via S-CE.

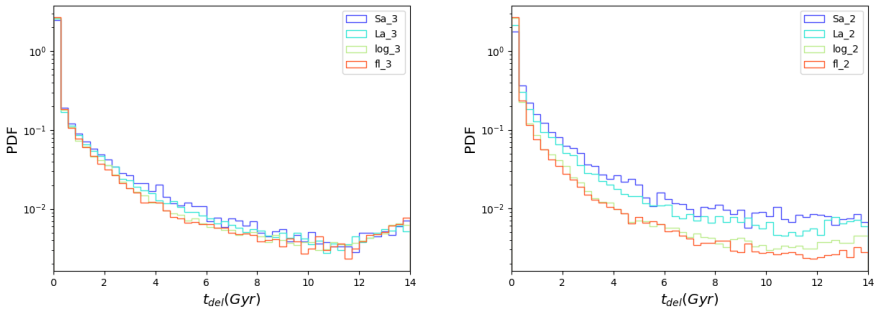

Figure 3.5: Compared $t_{\rm del}$ distribution from all the implemented IMFs coupled with (left) StacyBromm q, intermediate P, thermal e (right) Sana q, short P, Sana e. In this comparison it is visible that the catalogue that assume StacyBromm q distribution experience an inversion of slope in the distribution of $t_{\rm del}$ above ~ 12 Gyr

Chirp mass

Determining the typical chirp mass expected from a pop III compact binary has important consequences on the intensity of the GW signal it can produce and, consequently, the detectability of its merger event. The distribution of the $M_{\rm chirp}$ for the different catalogues - calculated from eq. 1.20 - is displayed in fig. 3.6, while in fig. 3.7 the distributions of the primary and secondary masses are plotted.

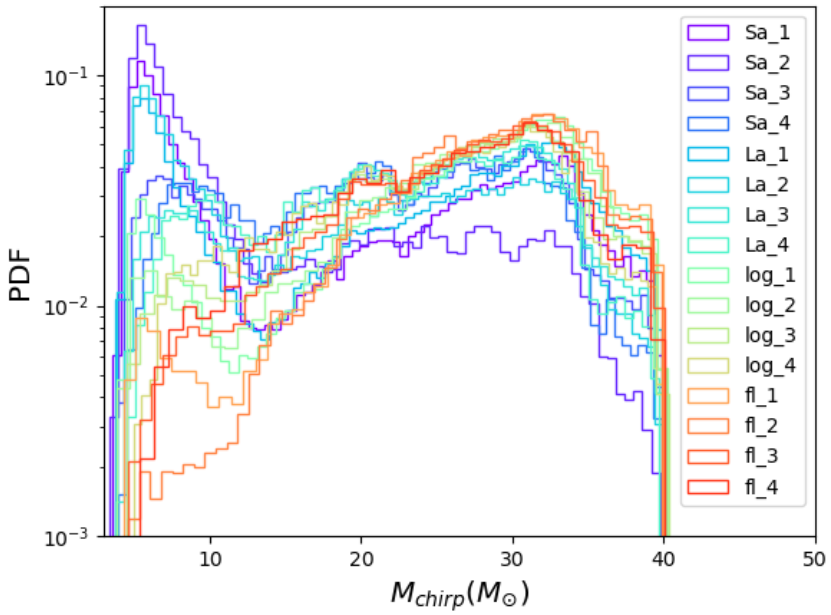

Figure 3.6: $M_{\rm chirp}$ distribution for all the catalogues generated by SEVN.

The catalogues present a typical chirp mass of ~ 30 M$_\odot$ and a maximum value of $M_{\rm chirp} \approx 40$ M$_\odot$, in agreement with previous results, e.g. (Kinugawa et al., 2014, 2016; Belczynski et al., 2017; Tanikawa et al., 2020). A second peak at low mass $M_{\rm chirp} < 10$ M$_\odot$ is also present in most of the catalogues, becoming dominant when $\alpha = -2.35$ IMF is assumed, owing to the abundance of low mass stars those IMFs.

The primary remnant mass distribution presents 2 sub-populations: one largely dominant that peaks at ~ 50 M$_\odot$ and has a maximum value ~ 60 M$_\odot$, and a second composed of few very massive objects above the pair instability mass gap with BH masses 240 M$_\odot$. This second sub-population is not present for secondary stars, which presents a distribution with two peaks, one at ~ 45 M$_\odot$ and another at $M_{2,BH} < 10$ M$_\odot$.

The explanation of the relatively low BH masses, despite the initial mass of the star was sampled up to 300 M$_\odot$, relies on the fact that all the system must experience stable or unstable mass transfer in order to reach coalescence within an Hubble time. Stable mass transfer, indeed, allows the systems to conserve most of their mass. To be able to avoid CE, however, the components need to be low mass stars ($M \lesssim 50$ M$_\odot$). If the systems instead do encounter a CE phase, the consequence is the ejection of the outer envelope and, therefore, the maximum BH mass achievable through this evolutionary channel is set by the

mass of stellar helium core (even in the case of direct collapse), which explains the BH mass range we obtain for our catalogues.

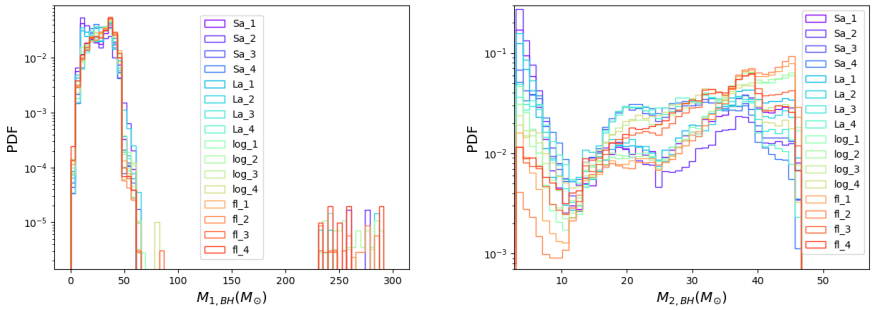

Figure 3.7: The distribution of primary (left) and secondary (right) BH masses for all the catalogues generated by SEVN. Except a non statistically relevant population of very massive stars (mainly present when the P distribution is long), all BHs present a mass < 50 $M_\odot$.

Another important aspect we can explore is the final distribution of semi-major axes for the compact binaries. In figure 3.8 we plot this distribution. Despite the typical initial semi major axis can vary by 3 orders of magnitude across the different catalogues, the final distribution of a is analogous for all of them and presents a steep peak in $a \sim 10$ $R_\odot$. This selection effect was expected since, as we already discussed, systems need to end their evolution as a close compact binary in order to reach merger within an Hubble time.

3.1.2 CosmoRate runs

In tab. 3.5 we report all the runs of CosmoRate we used for our model comparison. Each run of CosmoRate combines the information of an input catalogue generated by SEVN with a chosen prescription for the SFRD for a total of 64 different models setup.

3.2 MRD

In fig. 3.9 we plotted the MRD from all the 64 runs we considered. As we saw, the merger rate density is obtained following the eq. 2.4, via a combination of SFRD, merger efficiency and time delay.

Most of the systems have a relatively short delay time and the merger efficiency is a constant for each catalogue, thus evolution of BBH's MRD closely follows the functional form of the SFRD used in its calculation. We can nonetheless see notable detachment from this functional form at low redshift - when pop

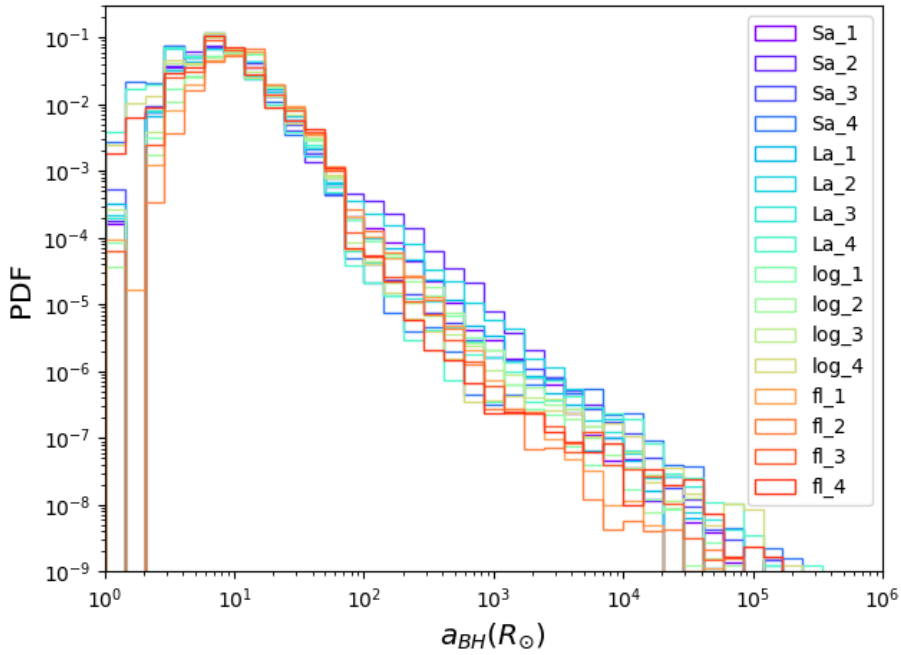

Figure 3.8: The distribution of semi major axes of the BBHs.

III star formation no longer takes place - and at high redshift, as after its formation, a system takes at least $\sim 10^7$ yr to generate a merger event.

We already discussed the different SFRD models in Section 2.1.1, while the similarity between them and the MRD they produce is highlighted in fig 3.10.

We can therefore conclude that the choice of the SFRD prescription is the one with the biggest impact on the MRD we obtain, determining the redshift at which the function peaks and the slope of the function above it.

The height of the peak, on the other hand, is largely determined by the merger efficiency. The merger efficiency, indeed, acts as a scale factor, varying by up order of magnitude the resulting MRD. As we discussed in the previous section, the values of η we found - reported in tab 3.3 - reflect the likelihood for a system to have a significant binary interaction and survive it to end its evolution in a tight compact binary.

In fig 3.11 we plotted the MRD choosing color based on the merger efficiency to highlight the behaviour just described. The value of the peck ranges from $\mathcal{R}(9) \simeq 129.18\text{Gpc}^{-1}\text{yr}^{-1}$ from Ds_La_3 to $\mathcal{R}(10) \simeq 0.66\text{Gpc}^{-1}\text{yr}^{-1}$ for Lb_fl_4.

The last term that enters in our calculation of the MRD is the delay time. Compared to the merger efficiency, the influence of a different time delay distribution is subdominant, causing a variation in the resulting MRD up to a factor

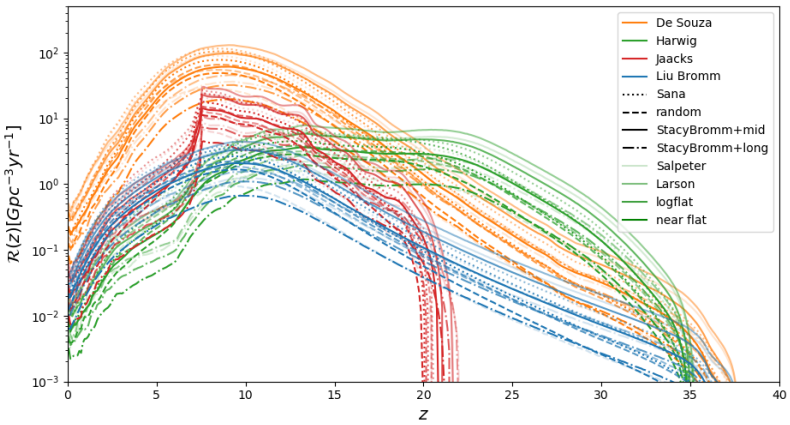

Figure 3.9: Visual comparison of the MRD from all the runs listed in tab. 3.5. The SFRD prescriptions assumed is distinguished by color: DeSouza in orange, Hartwig in green, Jaacks in red, LiuBromm in blue (name of the models refers to tab. 3.5); the IMF are distinguished by the shade, from the more to the less faint: Salpeter, Larson, logflat, near-flat (name of the models refers to tab 3.1); the mass ratio distribution prescriptions are distinguished by the line style: Sana is the dotted line, random is the dashed line, StacyBromm is the solid line (name of the models refers to tab 3.1). Note that the runs that use Sana or random prescriptions for the mass ratio distribution also use short Period and Sana eccentricity distribution. The runs that use StacyBromm mass ratio distribution are coupled with mid or long period and thermal eccentricity distributions, as reported in tab 3.5.

~ 3. Here we investigate how $t_{\rm del}$ comes into play in determining the MRD, dividing the discussion into tree regimes: (1) the high redshift tale ($z > 15$), (2) the peak ($z \sim 10$),(3) the behaviour at low redshift ($z < 5$).

The high redshift tale is the regime we are less interested in, given that even the most powerful future instrumentation will not be able to observe at such high redshift. Nonetheless this is the regime in which catalogues show the biggest discrepancies caused by the $t_{\rm del}$ distortion. For the catalogues that use StacyBromm mass ratio distribution - coupled with long or intermediate periods distribution and thermal eccentricity distribution, Sa_3, La_3, log_3, fl_3, Sa_4, La_4, log_4 and fl_4 - the impact of the $t_{\rm del}$ distribution increases the MRD by a factor ~ 3 with respect to the other catalogues.

The reason for this behaviour is probably to be attributed to the abundance of massive and eccentric binaries tend to experience interaction due to close encounter between the components, that strongly perturb the system's equilibrium and provoke its coalescence at low $t_{\rm del}$. The IMF in this regime plays a minor role, where a steeper mass distribution results in a slightly higher MRD, proba-

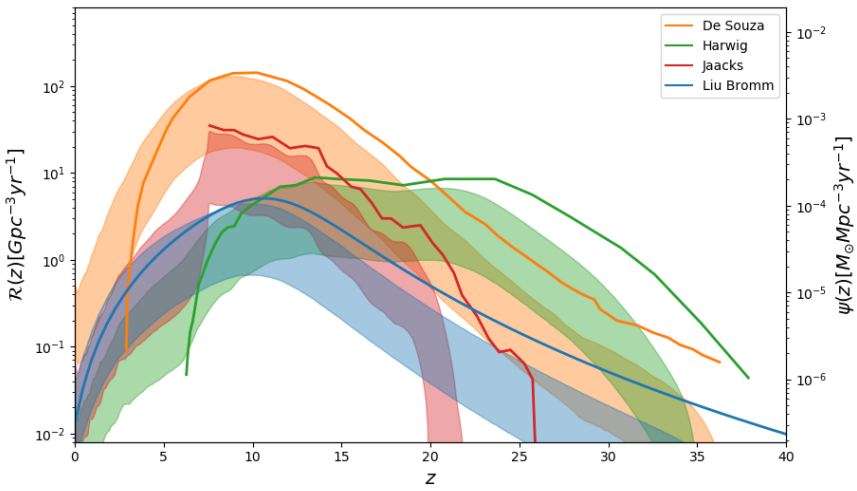

Figure 3.10: A superposition of the MRD and the SFRD. The solid lines are the various SFRD prescriptions while the filled regions contain all the MRDs obtained using each SFRD prescription.

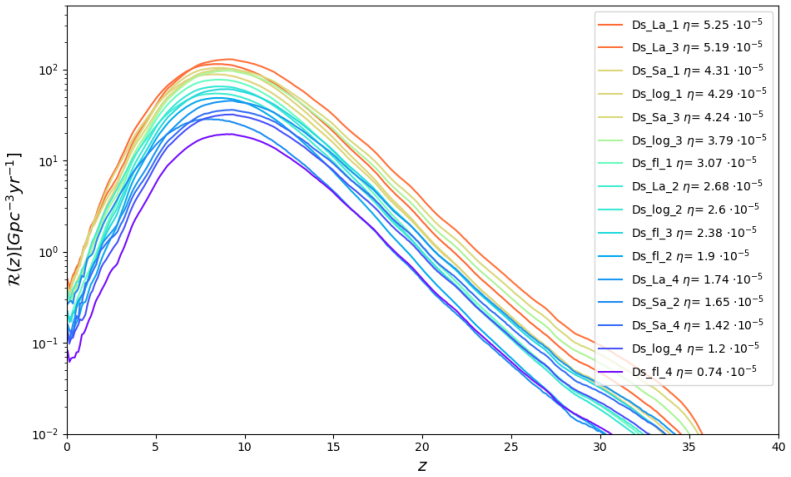

Figure 3.11: The MRD assuming DeSouza SFRD prescription. The color for each model is related to the corresponding merger efficiency.

bly correlated with the higher recurrence of core-collapse supernovae, which can alter the binary parameter and lead to an earlier merger.

The peak of the distribution is barely affected by the distribution of delay times. When a flatter IMF is assumed, the peak appears slightly higher in value and shifted toward higher redshift. The effect is nonetheless barely noticeable (less than a factor 2 in the value of MRD and shifted up to a redshift ~ 1).

At low redshift the formation of new pop III stars terminate, and the MRD is driven by the high $t_{\rm del}$ systems. In this regime, if we do not consider the merger efficiency, the dominant factor appears to be the IMF, since the models that favors lower mass stars have a higher percentage of stable mass transfer and low mass S-CE systems (as we show in tab. 3.6) that drive up the number of mergers at $z \lesssim 5$. The mass ratio distribution also plays a role in this context, since systems which present a huge mass gap between their components rarely survive longer than $\sim 10^8$ yr and therefore return a lower value of the MRD in this regime.

At $z = 0$ we find $\mathcal{R}(0) \in [0.003, 0.5] \mathrm{Gpc}^{-1}\mathrm{yr}^{-1}$ between all the models. This result is consistent with previous works (Inayoshi et al., 2016; Kinugawa et al., 2020; Tanikawa et al., 2021; Hijikawa et al., 2021) and with the observational constrains on the MRD (pop I/II + pop III) from (The LIGO Scientific Collaboration et al., 2021).

Another extremely important question we want to investigate is the redshift at which pop III MRD becomes dominant when compared to the pop I/II MRD. To answer this question we adopted Cosmo$\mathcal{R}$ate to calculate the MRD from a set of catalogues of pop I/II binaries, generated using SEVN with different metallicities. For this calculation we set $f_{\rm bin} = 0.4$ and $f_{\rm IMF} = 0.285$[2], we started the pop I/II star formation at $z = 15$ and assumed that at each $z-$bin the metallicity is distributed as a log-normal with $\sigma = 0.2$ and mean $u(z)$, where $u(z)$ is the average stellar metallicity as a function of redshift from (Madau & Fragos, 2017). In fig. 3.12 we show the comparison between the pop I/II MRD obtained with this setup and our pop III MRD. The transitional redshift is mainly determined by the SFRD prescription assumed and his value can widely vary.

Looking at the extremes, the most optimistic model (Ds_La_3) predict that pop III BBHs dominate the the overall number of merger events from $z \sim 5$. In this scenario the next generation of gravitational waves detectors will be able to observe a overall MRD which presents two peak: the highest from pop I/II systems and a second one at higher redshift, provided by pop III BBH mergers. To the other extreme, for the most pessimistic model (Lb_fl_4) pop III BBHs become the dominant source of merging events only the where the pop I/II star formation does not take place (above $z \sim 15$ in our pop I/II model). In this case pop III systems are only marginally relevance for future gravitational waves observational campaign.

[2]The primary mass was sampled from a Kroupa IMF (Kulczycki et al., 2006) in the range $5 - 150$ $\mathrm{M}_\odot$ and the secondary in the range $2.2 - 150$ $\mathrm{M}_\odot$. $f_{\rm IMF} = 0.285$ since the sampling mass range is not the entire mass range in witch pop I/II stars can be found (e.g. for primary we are neglecting the all the pop I/II stars with mass $\in [0.1, 5]$ $\mathrm{M}_\odot$)

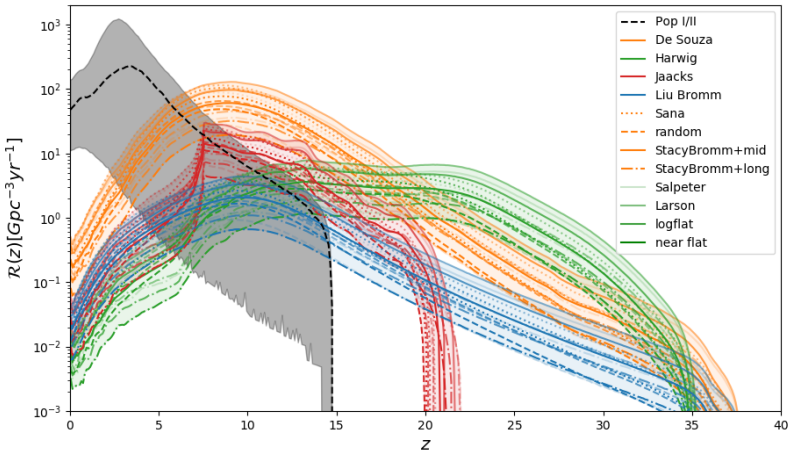

Figure 3.12: Same as fig. 3.9, now with the addiction of the MRD for pop I/II. The dash-dotted line represents median value over 1000 interactions while the filled grey region lies between the 25 and the 75 percentile.

3.3 Chirp mass evolution

Finally, we want to investigate how the typical chirp mass of the merging systems change with respect to the merging redshift. Understanding the $M_{\rm chirp}$ we expected from a merging a pop III BBH is crucial to distinguish the GW events with this origin from the events generated by later population binaries.

In fig 3.13 we plotted the evolution with respect to the redshift of the mean $M_{\rm chirp}$ and the distribution of $M_{\rm chirp}$ from the systems that merge in the local Universe ($z < 2$). In the plots we always use the same SFRD prescription since changing this prescription does not shows any significant effect.

It is interesting to notice how steeper IMFs predict an increase of $M_{\rm chirp}$ with increasing redshift, from $\sim$ 10 $M_\odot$ at $z \sim 0$ to $\sim$ 20 $M_\odot$ at $z \sim 30$. Flatter IMFs, on the other hand, return a relatively constant mean value of $M_{\rm chirp} \sim 25-28$ $M_\odot$ across a large range of redshift, $z \sim 0-30$. We can explain this behaviour by looking at the main evolutionary channel at low Z, as shown in tab 3.6. The catalogue that experience the most noticeable variation of mean $M_{\rm chirp}$ correspond with the catalogue that presents the highest percentage of stable mass transfer at low z. The system that experience no CE are usually less massive. Moreover, below the $M_{\rm ZAMS}$ threshold of $\sim$ 40 $M_\odot$ the components of the system end their life in a core-collapse SN, losing considerably more mass that a star that experience direct-collapse. We therefore conclude that the abundance of systems that evolve without experiencing CE contribute in lowering the mean $M_{\rm chirp}$.

The evolutionary channel changes from tab. 3.4 - that account for the entire

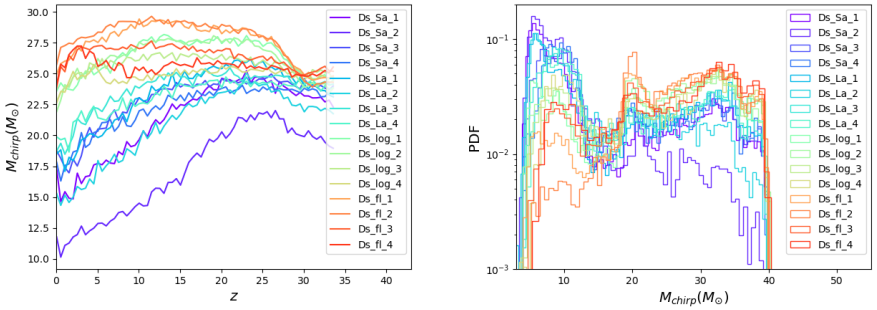

Figure 3.13: Left: the evolution of the mean chirp mass with redshift, we only plot the model with DeSouza SFRD prescription because the SFRD does not affect the evolution significantly. Right: the distribution of chirp mass for events that take pace at $z < 2$. The distribution obtained does not deviate significantly from the one obtained using the whole catalogues (fig. 3.6).

catalogue of objects - to tab. 3.6 - that account for objects with $t_{\rm del} > 3$ Gyr -.

If we consider only the systems with $t_{\rm del} > 3$ Gyr (tab. 3.6) the recurrence of evolutionary channel changes significantly with respect to tab. 3.4, calculated using the entire catalogue of objects. This behavior, nonetheless, does not alter the distribution of $M_{\rm chirp}$ at low z - displayed in fig 3.13 for $z < 2$-. It indeed resembles the distribution calculated from the whole catalogues (fig. 3.6). Also in this case we found a lower peak at $M_{\rm chirp} \sim 10$ M$_\odot$ - mainly from catalogues that assume steeper IMF - and a higher peak around $M_{\rm chirp} \sim 30$ M$_\odot$, more relevant for catalogues that assume flatter IMF.

Scheme of all the Cosmo$\mathcal{R}$ate simulation runs					
Name	SFRD	IMF	q	P	e
Ds_Sa_1	DeSouza	Salpeter	Sana	short	Sana
Ds_Sa_2	DeSouza	Salpeter	random	short	Sana
Ds_Sa_3	DeSouza	Salpeter	StacyBromm	mid	thermal
Ds_Sa_4	DeSouza	Salpeter	StacyBromm	long	thermal
Ds_La_1	DeSouza	Larson	Sana	short	Sana
Ds_La_2	DeSouza	Larson	random	short	Sana
Ds_La_3	DeSouza	Larson	StacyBromm	mid	thermal
Ds_La_4	DeSouza	Larson	StacyBromm	long	thermal
Ds_log_1	DeSouza	logflat	Sana	short	Sana
Ds_log_2	DeSouza	logflat	random	short	Sana
Ds_log_3	DeSouza	logflat	StacyBromm	mid	thermal
Ds_log_4	DeSouza	logflat	StacyBromm	long	thermal
Ds_fl_1	DeSouza	near-flat	Sana	short	Sana
Ds_fl_2	DeSouza	near-flat	random	short	Sana
Ds_fl_3	DeSouza	near-flat	StacyBromm	mid	thermal
Ds_fl_4	DeSouza	near-flat	StacyBromm	long	thermal
Ht_Sa_1	Hartwig	Salpeter	Sana	short	Sana
Ht_Sa_2	Hartwig	Salpeter	random	short	Sana
Ht_Sa_3	Hartwig	Salpeter	StacyBromm	mid	thermal
Ht_Sa_4	Hartwig	Salpeter	StacyBromm	long	thermal
Ht_La_1	Hartwig	Larson	Sana	short	Sana
Ht_La_2	Hartwig	Larson	random	short	Sana
Ht_La_3	Hartwig	Larson	StacyBromm	mid	thermal
Ht_La_4	Hartwig	Larson	StacyBromm	long	thermal
Ht_log_1	Hartwig	logflat	Sana	short	Sana
Ht_log_2	Hartwig	logflat	random	short	Sana
Ht_log_3	Hartwig	logflat	StacyBromm	mid	thermal
Ht_log_4	Hartwig	logflat	StacyBromm	long	thermal
Ht_fl_1	Hartwig	near-flat	Sana	short	Sana
Ht_fl_2	Hartwig	near-flat	random	short	Sana
Ht_fl_3	Hartwig	near-flat	StacyBromm	mid	thermal
Ht_fl_4	Hartwig	near-flat	StacyBromm	long	thermal
Ja_Sa_1	Jaacks	Salpeter	Sana	short	Sana
Ja_Sa_2	Jaacks	Salpeter	random	short	Sana
Ja_Sa_3	Jaacks	Salpeter	StacyBromm	mid	thermal
Ja_Sa_4	Jaacks	Salpeter	StacyBromm	long	thermal
Ja_La_1	Jaacks	Larson	Sana	short	Sana
Ja_La_2	Jaacks	Larson	random	short	Sana
Ja_La_3	Jaacks	Larson	StacyBromm	mid	thermal
Ja_La_4	Jaacks	Larson	StacyBromm	long	thermal
Ja_log_1	Jaacks	logflat	Sana	short	Sana
Ja_log_2	Jaacks	logflat	random	short	Sana
Ja_log_3	Jaacks	logflat	StacyBromm	mid	thermal
Ja_log_4	Jaacks	logflat	StacyBromm	long	thermal
Ja_fl_1	Jaacks	near-flat	Sana	short	Sana
Ja_fl_2	Jaacks	near-flat	random	short	Sana
Ja_fl_3	Jaacks	near-flat	StacyBromm	mid	thermal
Ja_fl_4	Jaacks	near-flat	StacyBromm	long	thermal
Lb_Sa_1	LiuBromm	Salpeter	Sana	short	Sana
Lb_Sa_2	LiuBromm	Salpeter	random	short	Sana
Lb_Sa_3	LiuBromm	Salpeter	StacyBromm	mid	thermal
Lb_Sa_4	LiuBromm	Salpeter	StacyBromm	long	thermal
Lb_La_1	LiuBromm	Larson	Sana	short	Sana
Lb_La_2	LiuBromm	Larson	random	short	Sana
Lb_La_3	LiuBromm	Larson	StacyBromm	mid	thermal
Lb_La_4	LiuBromm	Larson	StacyBromm	long	thermal
Lb_log_1	LiuBromm	logflat	Sana	short	Sana
Lb_log_2	LiuBromm	logflat	random	short	Sana
Lb_log_3	LiuBromm	logflat	StacyBromm	mid	thermal
Lb_log_4	LiuBromm	logflat	StacyBromm	long	thermal
Lb_th_1	LiuBromm	near-flat	Sana	short	Sana
Lb_th_2	LiuBromm	near-flat	random	short	Sana
Lb_th_3	LiuBromm	near-flat	StacyBromm	mid	thermal
Lb_th_4	LiuBromm	near-flat	StacyBromm	long	thermal

Table 3.5: Summary table of all the simulation runs made for this thesis and the models of SFRD, IMF and binary properties assumed for each run. For the SFRD, the model DeSouza refers to the model present in (de Souza et al., 2011), Hartwig refers to the model present in (Hartwig, Volonteri, et al., 2016), Jaacks refers to the model present in (Jaacks et al., 2019), LiuBromm refers to the model present in (Liu & Bromm, 2020a)

Evolutionary channel recurrence					
Cat.	No-CE (%)	P-CE (%)	S-CE (%)	D-CE (%)	2-CE (%)
Sa_1	15.9	2.6	63.3	17.3	0.9
Sa_2	30.4	7.1	57.6	3.7	1.2
Sa_3	4.3	7.7	66.1	20.0	1.9
Sa_4	2.5	7.7	61.7	23.3	4.8
La_1	14.8	3.2	56.5	23.8	1.7
La_2	24.8	9.3	55.5	9.0	1.5
La_3	3.6	10.2	58.3	24.9	2.9
La_4	2.4	9.3	53.8	30.8	3.8
log_1	8.6	4.5	38.9	42.8	5.2
log_2	10.5	10.4	35.7	35.5	7.8
log_3	2.9	12.6	33.2	44.3	6.9
log_4	1.5	13.6	28.9	46.3	9.7
fl_1	4.5	4.8	28.7	51.1	10.9
fl_2	1.8	4.2	23.3	53.2	17.5
fl_3	1.3	13.5	19.8	53.9	11.4
fl_4	0.8	13.3	13.2	57.5	15.2

Table 3.6: Similar to tab 3.4 but limited to $t_{\rm del} > 3$ Gyr, which roughly correspond to the population that formed at redshift $z \sim 10$, the SFRD peak, and merge at $z \gtrsim 2$ (the detection horizon of LIGO-Virgo). For each Input catalogue, the fraction of binary that do not experience CE (No-CE), that experience a single CE with the primary in giant branch (P-CE), with the secondary in giant branch (S-CE), with both the components giant branch (D-CE) or that experience two CE phases (2-CE). The percentage of No-CE increase considerably with respect to tab. 3.4 since typically the systems that experience this evolutionary channel have long $t_{\rm del}$

Chapter 4

Conclusions

In this thesis, we estimated the merger rate density of BBHs with pop III origin, and investigated how it is affected by the uncertainties about the SFRD, IMF and distribution of mass ratio, orbital period and eccentricity for pop III binaries.

We used the population syntheses code SEVN to generate a set of catalogues of BBHs that merge within an Hubble time. For each catalogue, the initial conditions of the systems - IMF, distribution of q, a and e - were sorted using a different set of prescriptions, in order to account for the lack of knowledge about pop III binary statistics. We than combined the information obtained from the catalogues with a function describing the pop III SFRD to calculate the pop III MRD using a customized version of the code Cosmo$\mathcal{R}$ate. Also for the SFRD, a variety of possible prescriptions were considered, since the theoretical models do not converge on a common prediction.

We obtained a total of 64 MRD functions and displayed them in fig. 3.9. Coupling this results with an analysis of the input catalogues allowed us to infer the influence of each model decision. The conclusion reached can be summarized as follows:

- The SFRD is the dominant source of uncertainty in the calculation of the MRD. The prescriptions implemented from existing work, in turns, largely depend on the interplay between the cooling mechanisms of the minihalo and the feedbacks from the stellar activity, as the former allows the stellar formation to take place and the latter suppresses the formation process. The SFRD model choice sets the redshift at which the mergers stats, the slope that the function follows up to its peak and the location of the peak itself;

- The IMF followed by the primary stars plays a subdominant role in the final calculation of the MRD. It's effect, indeed, is linked to the distribution of delay time, especially towards low redshift ($z \lesssim 5$) but, is never relevant enough to drive the overall trend of the results. A correlation between the slope of the mass distribution assumed and the MRD obtained

is nonetheless present: an IMF with steep negative slope return higher values of the MRD with respect to a flatter - thus more top-heavy - IMF. In addition, the presence of a lower mass cut for $M_{\rm ZAMS} < 20$ M$_\odot$ in the Larson IMF prescription produces a more optimistic MRD if compared to a Saltpeter IMF, which has the same slope of the distribution but no cut;

- The combination of mass ratio and semi major axis distribution have, instead, an high relevance in determining the MRD, mainly owing to their impact on the merger efficiency. The models that create the most favorable condition for an efficient BBH production are (1) the models that couple small semi major axes and high mass ratios and (2) the models that couple moderate semi major axes and low mass ratios. The former produces the most optimistic MRD at low redshift while the latter returns the highest results at high redshift. On the opposite side, the most pessimistic models combine large semi major axes with low mass ratios, discouraging both the occurrence of binary interactions and the probability of survival;

- The only impact that the distribution of initial eccentricity has on the MRD emerges when it is coupled with long orbital period distribution. Indeed, as the typical size of the orbit increases, the systems that manage to have significant binary interactions tend to be the one with high eccentricity. In all the other cases the initial eccentricity distributions have a negligible effect on the MRD, since the systems quickly lose the memory of this parameter during their evolution;

- The primary means by which binary initial conditions distribution exert their influence on the delay time distribution and the merger efficiency is by altering the statistical occurrence of the evolutionary channels that allow the systems to reach merger within an Hubble time.

To carry out our investigation we made several simplifying assumptions. Further studies can overcome this simplifications and expand our model comparison, updating the stellar evolution model and considering a larger set of binary initial conditions. Some of the most relevant improvements this work can benefit from are:

- The development of a dedicated set of evolutionary tracks to simulate the evolution of pop III stars with SEVN. For our model comparison we simulated all the systems at fixed metallicity ($Z = 0.0001$). Nonetheless, the typical metallicity of pop III stars is expected to be $Z \lesssim 10^{-8}$ (Schneider et al., 2006). A lower initial metallicity may affect the nuclear burning evolution, the stellar radius, the temperature, the core mass and the giant evolution, among other aspects. Binary interactions can be significantly altered as a consequence. The development of pop III evolutionary tracks opens the possibility to explore the aspect that distinguish the events with pop III origin from the ones generated from pop I/II systems. In addition, with a set of extremely low metallicity tacks (up to $Z = 0$) it is possible to introduce a prescription for the high redshift metallicity evolution of

the medium (for $z \sim 35 - 7$) in the calculation of pop III MRD. This implementation therefore constitutes the most important next step in our investigation;

- The implementation of a mass-dependent fraction of binaries. The binary fraction for pop III stars is a poorly understood aspect. The observation on pop I/II stars, nonetheless, suggests correlation between binary fraction and mass. The implementation of the functional behavior of $f_{\rm bin}$ can enable to study the possible influence it could have on the MRD;

- The extension of the model comparison to additional binary initial conditions such as components rotation and magnetic field. We did not consider the impact of rotation and magnetic fields in our investigation, nonetheless they may play a relevant role in determining the mass evolution on the systems binaries interactions. It is thus important to include them in a future implementation of the model comparison.

Moreover, the studies of pop III stars and of gravitational waves from astrophysical objects are growing at a fast pace. The increase in computational power will allow to improve the resolution and the accuracy of the cosmological simulation, providing new boundaries on SFRD and binary statistic. Alongside the theoretical achievements, the new generation of gravitational wave detectors will be able to detect events from regions of the Universe never reached before, providing new observation constraints for the merger rate density. When this new information will be available, it will be possible to adopt our work as a base framework to infer crucial information on the physics of pop III binary systems via Bayesian analysis.

References

Abbott, B. P., Abbott, R., Abbott, T. D., Abernathy, M. R., Acernese, F., Ackley, K., ... Virgo Collaboration (2016, February). Observation of Gravitational Waves from a Binary Black Hole Merger. , *116*(6), 061102. doi: 10.1103/PhysRevLett.116.061102

Abel, T., Anninos, P., Zhang, Y., & Norman, M. L. (1997, August). Modeling primordial gas in numerical cosmology. , *2*(3), 181-207. doi: 10.1016/S1384-1076(97)00010-9

Abel, T., Bryan, G. L., & Norman, M. L. (2000, September). The Formation and Fragmentation of Primordial Molecular Clouds. *Astrophysical Journal*, *540*(1), 39-44. doi: 10.1086/309295

Abel, T., Bryan, G. L., & Norman, M. L. (2002, January). The Formation of the First Star in the Universe. *Science*, *295*(5552), 93-98. doi: 10.1126/science.295.5552.93

Abel, T., & Haiman, Z. (2000, January). The Role of H_2 Molecules in Cosmological Structure Formation. In F. Combes & G. Pineau Des Forets (Eds.), *Molecular hydrogen in space* (p. 237).

Abt, H. A. (1983, January). Normal and abnormal binary frequencies. , *21*, 343-372. doi: 10.1146/annurev.aa.21.090183.002015

Amaro-Seoane, P., Audley, H., Babak, S., & Baker, J. e. a. (2017, February). Laser Interferometer Space Antenna. *arXiv e-prints*, arXiv:1702.00786.

Banik, N., Tan, J. C., & Monaco, P. (2019, March). The formation of supermassive black holes from Population III.1 seeds. I. Cosmic formation histories and clustering properties. *Monthly Notices*, *483*(3), 3592-3606. doi: 10.1093/mnras/sty3298

Baraffe, I., Heger, A., & Woosley, S. E. (2001, April). On the Stability of Very Massive Primordial Stars. *Astrophysical Journal*, *550*(2), 890-896. doi: 10.1086/319808

Barkana, R., & Loeb, A. (2001, July). In the beginning: the first sources of light and the reionization of the universe. , *349*(2), 125-238. doi: 10.1016/S0370-1573(01)00019-9

Belczynski, K., Bulik, T., Fryer, C. L., Ruiter, A., Valsecchi, F., Vink, J. S., & Hurley, J. R. (2010, May). On the Maximum Mass of Stellar Black Holes. *Astrophysical Journal*, *714*(2), 1217-1226. doi: 10.1088/0004-637X/714/2/1217

Belczynski, K., Bulik, T., & Rudak, B. (2004, June). The First Stellar Binary Black Holes: The Strongest Gravitational Wave Burst Sources. , *608*(1), L45-L48. doi: 10.1086/422172

Belczynski, K., Dominik, M., Bulik, T., O'Shaughnessy, R., Fryer, C., & Holz, D. E. (2010, June). The Effect of Metallicity on the Detection Prospects for Gravitational Waves. , *715*(2), L138-L141. doi: 10.1088/2041-8205/715/2/L138

Belczynski, K., Ryu, T., Perna, R., Berti, E., Tanaka, T. L., & Bulik, T. (2017, November). On the likelihood of detecting gravitational waves from Population III compact object binaries. *Monthly Notices*, *471*(4), 4702-4721. doi: 10.1093/mnras/stx1759

Bernardeau, F., Colombi, S., Gaztañaga, E., & Scoccimarro, R. (2002, September). Large-scale structure of the Universe and cosmological perturbation theory. , *367*(1-3), 1-248. doi: 10.1016/S0370-1573(02)00135-7

Bond, H. E. (1980, September). Where is Population III? In *Bulletin of the american astronomical society* (Vol. 12, p. 831).

Bressan, A., Marigo, P., Girardi, L., Salasnich, B., Dal Cero, C., Rubele, S., & Nanni, A. (2012, November). PARSEC: stellar tracks and isochrones with the PAdova and TRieste Stellar Evolution Code. *Monthly Notices*, *427*(1), 127-145. doi: 10.1111/j.1365-2966.2012.21948.x

Bromm, V., Coppi, P. S., & Larson, R. B. (1999, December). Forming the First Stars in the Universe: The Fragmentation of Primordial Gas. , *527*(1), L5-L8. doi: 10.1086/312385

Bromm, V., Coppi, P. S., & Larson, R. B. (2002, January). The Formation of the First Stars. I. The Primordial Star-forming Cloud. *Astrophysical Journal*, *564*(1), 23-51. doi: 10.1086/323947

Bromm, V., & Larson, R. B. (2004, September). The First Stars. , *42*(1), 79-118. doi: 10.1146/annurev.astro.42.053102.134034

Chen, Y., Bressan, A., Girardi, L., Marigo, P., Kong, X., & Lanza, A. (2015, September). PARSEC evolutionary tracks of massive stars up to 350 $M_{\odot}$ at metallicities $0.0001 \leq Z \leq 0.04$. *Monthly Notices*, *452*(1), 1068-1080. doi: 10.1093/mnras/stv1281

Ciardi, B., & Ferrara, A. (2005, February). The First Cosmic Structures and Their Effects. , *116*(3-4), 625-705. doi: 10.1007/s11214-005-3592-0

Ciardi, B., Ferrara, A., & Abel, T. (2000, April). Intergalactic H_2 Photodissociation and the Soft Ultraviolet Background Produced by Population III Objects. *Astrophysical Journal*, *533*(2), 594-600. doi: 10.1086/308673

Clark, P. C., Glover, S. C. O., Klessen, R. S., & Bromm, V. (2011, February). Gravitational Fragmentation in Turbulent Primordial Gas and the Initial Mass Function of Population III Stars. *Astrophysical Journal*, *727*(2), 110. doi: 10.1088/0004-637X/727/2/110

de Mink, S. E., & Belczynski, K. (2015, November). Merger Rates of Double Neutron Stars and Stellar Origin Black Holes: The Impact of Initial Conditions on Binary Evolution Predictions. *Astrophysical Journal*, *814*(1), 58. doi: 10.1088/0004-637X/814/1/58

de Souza, R. S., Yoshida, N., & Ioka, K. (2011, September). Populations III.1 and III.2 gamma-ray bursts: constraints on the event rate for future radio and X-ray surveys. *Astronomy & Astrophysics*, *533*, A32. doi: 10.1051/0004-6361/201117242

Dominik, M., Belczynski, K., Fryer, C., Holz, D. E., Berti, E., Bulik, T., ... O'Shaughnessy, R. (2012, November). Double Compact Objects. I. The Significance of the Common Envelope on Merger Rates. *Astrophysical Journal*, *759*(1), 52. doi: 10.1088/0004-637X/759/1/52

Dominik, M., Belczynski, K., Fryer, C., Holz, D. E., Berti, E., Bulik, T., ... O'Shaughnessy, R. (2013, December). Double Compact Objects. II. Cosmological Merger Rates. *Astrophysical Journal*, *779*(1), 72. doi: 10.1088/0004-637X/779/1/72

Duquennoy, A., & Mayor, M. (1991, August). Multiplicity among Solar Type Stars in the Solar Neighbourhood - Part Two - Distribution of the Orbital Elements in an Unbiased Sample. *Astronomy & Astrophysics*, *248*, 485.

Eggleton, P. P. (1983, May). Aproximations to the radii of Roche lobes. *Astrophysical Journal*, *268*, 368-369. doi: 10.1086/160960

Fryer, C. L. (1999, September). Mass Limits For Black Hole Formation. *Astrophysical Journal*, *522*(1), 413-418. doi: 10.1086/307647

Fryer, C. L., Belczynski, K., Wiktorowicz, G., Dominik, M., Kalogera, V., & Holz, D. E. (2012, April). Compact Remnant Mass Function: Dependence on the Explosion Mechanism and Metallicity. *Astrophysical Journal*, *749*(1), 91. doi: 10.1088/0004-637X/749/1/91

Glover, S. (2005, April). The Formation Of The First Stars In The Universe. , *117*(3-4), 445-508. doi: 10.1007/s11214-005-5821-y

Glover, S. (2013, January). The First Stars. In T. Wiklind, B. Mobasher, & V. Bromm (Eds.), *The first galaxies* (Vol. 396, p. 103). doi: 10.1007/978-3-642-32362-1_3

Gnedin, N. Y., & Hui, L. (1998, May). Probing the Universe with the Lyalpha forest - I. Hydrodynamics of the low-density intergalactic medium. *Monthly Notices*, *296*(1), 44-55. doi: 10.1046/j.1365-8711.1998.01249.x

Greif, T. H. (2015, March). The numerical frontier of the high-redshift Universe. *Computational Astrophysics and Cosmology*, *2*, 3. doi: 10.1186/s40668-014-0006-2

Greif, T. H., & Bromm, V. (2006, November). Two populations of metal-free stars in the early Universe. *Monthly Notices*, *373*(1), 128-138. doi: 10.1111/j.1365-2966.2006.11017.x

Greif, T. H., Bromm, V., Clark, P. C., Glover, S. C. O., Smith, R. J., Klessen, R. S., ... Springel, V. (2012, July). Formation and evolution of primordial protostellar systems. *Monthly Notices*, *424*(1), 399-415. doi: 10.1111/j.1365-2966.2012.21212.x

Haiman, Z., Abel, T., & Rees, M. J. (2000, May). The Radiative Feedback of the First Cosmological Objects. *Astrophysical Journal*, *534*(1), 11-24. doi: 10.1086/308723

Hartwig, T., Bromm, V., Klessen, R. S., & Glover, S. C. O. (2015, March). Constraining the primordial initial mass function with stellar archaeology.

Monthly Notices, *447*(4), 3892-3908. doi: 10.1093/mnras/stu2740

Hartwig, T., Latif, M. A., Magg, M., Bromm, V., Klessen, R. S., Glover, S. C. O., ... Volonteri, M. (2016, October). Exploring the nature of the Lyman-α emitter CR7. *Monthly Notices*, *462*(2), 2184-2202. doi: 10.1093/mnras/stw1775

Hartwig, T., Volonteri, M., Bromm, V., Klessen, R. S., Barausse, E., Magg, M., & Stacy, A. (2016, July). Gravitational waves from the remnants of the first stars. *Monthly Notices*, *460*(1), L74-L78. doi: 10.1093/mnrasl/slw074

Heger, A., Fryer, C. L., Woosley, S. E., Langer, N., & Hartmann, D. H. (2003, July). How Massive Single Stars End Their Life. *Astrophysical Journal*, *591*(1), 288-300. doi: 10.1086/375341

Heger, A., & Woosley, S. E. (2010, November). Nucleosynthesis and Evolution of Massive Metal-free Stars. *Astrophysical Journal*, *724*(1), 341-373. doi: 10.1088/0004-637X/724/1/341

Heger, A., Woosley, S. E., Fryer, C. L., & Langer, N. (2003, January). Massive Star Evolution Through the Ages. In W. Hillebrandt & B. Leibundgut (Eds.), *From twilight to highlight: The physics of supernovae* (p. 3). doi: 10.1007/10828549_1

Heggie, D. C. (1975, December). Binary evolution in stellar dynamics. *Monthly Notices*, *173*, 729-787. doi: 10.1093/mnras/173.3.729

Hijikawa, K., Tanikawa, A., Kinugawa, T., Yoshida, T., & Umeda, H. (2021, July). On the population III binary black hole mergers beyond the pair-instability mass gap. *Monthly Notices*, *505*(1), L69-L73. doi: 10.1093/mnrasl/slab052

Hirano, S., Hosokawa, T., Yoshida, N., Omukai, K., & Yorke, H. W. (2015, March). Primordial star formation under the influence of far ultraviolet radiation: 1540 cosmological haloes and the stellar mass distribution. *Monthly Notices*, *448*(1), 568-587. doi: 10.1093/mnras/stv044

Hirano, S., Hosokawa, T., Yoshida, N., Umeda, H., Omukai, K., Chiaki, G., & Yorke, H. W. (2014, February). One Hundred First Stars: Protostellar Evolution and the Final Masses. *Astrophysical Journal*, *781*(2), 60. doi: 10.1088/0004-637X/781/2/60

Hobbs, G., Lorimer, D. R., Lyne, A. G., & Kramer, M. (2005, July). A statistical study of 233 pulsar proper motions. *Monthly Notices*, *360*(3), 974-992. doi: 10.1111/j.1365-2966.2005.09087.x

Hopkins, P. F. (2015, June). A new class of accurate, mesh-free hydrodynamic simulation methods. *Monthly Notices*, *450*(1), 53-110. doi: 10.1093/mnras/stv195

Hurley, J. R., Pols, O. R., & Tout, C. A. (2000, July). Comprehensive analytic formulae for stellar evolution as a function of mass and metallicity. *Monthly Notices*, *315*(3), 543-569. doi: 10.1046/j.1365-8711.2000.03426.x

Hurley, J. R., Tout, C. A., & Pols, O. R. (2002, February). Evolution of binary stars and the effect of tides on binary populations. *Monthly Notices*, *329*(4), 897-928. doi: 10.1046/j.1365-8711.2002.05038.x

Hut, P. (1981, June). Tidal evolution in close binary systems. *Astronomy & Astrophysics*, *99*, 126-140.

Inayoshi, K., Hirai, R., Kinugawa, T., & Hotokezaka, K. (2017, July). Formation pathway of Population III coalescing binary black holes through stable mass transfer. *Monthly Notices*, *468*(4), 5020-5032. doi: 10.1093/mnras/stx757

Inayoshi, K., Kashiyama, K., Visbal, E., & Haiman, Z. (2016, September). Gravitational wave background from Population III binary black holes consistent with cosmic reionization. *Monthly Notices*, *461*(3), 2722-2727. doi: 10.1093/mnras/stw1431

Ivanova, N., Justham, S., Chen, X., De Marco, O., Fryer, C. L., Gaburov, E., ... Webbink, R. F. (2013, February). Common envelope evolution: where we stand and how we can move forward. , *21*, 59. doi: 10.1007/s00159-013-0059-2

Jaacks, J., Finkelstein, S. L., & Bromm, V. (2019, September). Legacy of star formation in the pre-reionization universe. *Monthly Notices*, *488*(2), 2202-2221. doi: 10.1093/mnras/stz1529

Jaacks, J., Thompson, R., Finkelstein, S. L., & Bromm, V. (2018, April). Baseline metal enrichment from Population III star formation in cosmological volume simulations. *Monthly Notices*, *475*(4), 4396-4410. doi: 10.1093/mnras/sty062

Jeans, J. H. (1902, January). The Stability of a Spherical Nebula. *Philosophical Transactions of the Royal Society of London Series A*, *199*, 1-53. doi: 10.1098/rsta.1902.0012

Jo, J. U., Youn, S., Kim, S., Park, Y., Hwang, J., Lee, J. H., & Kim, G. (2021, February). Star formation rate density across the cosmic time. , *366*(2), 18. doi: 10.1007/s10509-021-03925-7

Johnson, J. L. (2010, May). Population III star clusters in the reionized Universe. *Monthly Notices*, *404*(3), 1425-1436. doi: 10.1111/j.1365-2966.2010.16351.x

Johnson, J. L., & Bromm, V. (2006, February). The cooling of shock-compressed primordial gas. *Monthly Notices*, *366*(1), 247-256. doi: 10.1111/j.1365-2966.2005.09846.x

Johnson, J. L., Dalla Vecchia, C., & Khochfar, S. (2013, January). The First Billion Years project: the impact of stellar radiation on the co-evolution of Populations II and III. *Monthly Notices*, *428*(3), 1857-1872. doi: 10.1093/mnras/sts011

Karlsson, T., Johnson, J. L., & Bromm, V. (2008, May). Uncovering the Chemical Signature of the First Stars in the Universe. *Astrophysical Journal*, *679*(1), 6-16. doi: 10.1086/533520

Kinugawa, T., Inayoshi, K., Hotokezaka, K., Nakauchi, D., & Nakamura, T. (2014, August). Possible indirect confirmation of the existence of Pop III massive stars by gravitational wave. *Monthly Notices*, *442*(4), 2963-2992. doi: 10.1093/mnras/stu1022

Kinugawa, T., Miyamoto, A., Kanda, N., & Nakamura, T. (2016, February). The detection rate of inspiral and quasi-normal modes of Population III

binary black holes which can confirm or refute the general relativity in the strong gravity region. *Monthly Notices*, *456*(1), 1093-1114. doi: 10.1093/mnras/stv2624

Kinugawa, T., Nakamura, T., & Nakano, H. (2020, November). Chirp mass and spin of binary black holes from first star remnants. *Monthly Notices*, *498*(3), 3946-3963. doi: 10.1093/mnras/staa2511

Kinugawa, T., Nakamura, T., & Nakano, H. (2021a, February). Formation of binary black holes similar to GW190521 with a total mass of $\sim$150 $M_{\odot}$ from Population III binary star evolution. *Monthly Notices*, *501*(1), L49-L53. doi: 10.1093/mnrasl/slaa191

Kinugawa, T., Nakamura, T., & Nakano, H. (2021b, June). Gravitational waves from Population III binary black holes are consistent with LIGO/Virgo O3a data for the chirp mass larger than $\sim$20 $M_{\odot}$. *Monthly Notices*, *504*(1), L28-L33. doi: 10.1093/mnrasl/slab032

Kippenhahn, R., & Weigert, A. (1994). *Stellar Structure and Evolution.*

Krtička, J., & Kubát, J. (2006, February). The winds of hot massive first stars. *Astronomy & Astrophysics*, *446*(3), 1039-1049. doi: 10.1051/0004-6361:20053289

Kudritzki, R. P. (2002, September). Line-driven Winds, Ionizing Fluxes, and Ultraviolet Spectra of Hot Stars at Extremely Low Metallicity. I. Very Massive O Stars. *Astrophysical Journal*, *577*(1), 389-408. doi: 10.1086/342178

Kulczycki, K., Bulik, T., Belczyński, K., & Rudak, B. (2006, December). VIRGO sensitivity to binary coalescences and the Population III black hole binaries. *Astronomy & Astrophysics*, *459*(3), 1001-1006. doi: 10.1051/0004-6361:20065080

Larson, R. B. (1999, December). The Stellar Initial Mass Function. In T. Nakamoto (Ed.), *Star formation 1999* (p. 336-340).

Liu, B., & Bromm, V. (2020a, June). Gravitational waves from Population III binary black holes formed by dynamical capture. *Monthly Notices*, *495*(2), 2475-2495. doi: 10.1093/mnras/staa1362

Liu, B., & Bromm, V. (2020b, September). When did Population III star formation end? *Monthly Notices*, *497*(3), 2839-2854. doi: 10.1093/mnras/staa2143

Liu, B., & Bromm, V. (2021, October). Gravitational waves from the remnants of the first stars in nuclear star clusters. *Monthly Notices*, *506*(4), 5451-5467. doi: 10.1093/mnras/stab2028

Liu, B., Meynet, G., & Bromm, V. (2021, February). Dynamical evolution of population III stellar systems and the resulting binary statistics. *Monthly Notices*, *501*(1), 643-663. doi: 10.1093/mnras/staa3671

Loeb, A., & Furlanetto, S. R. (2013). *The First Galaxies in the Universe.*

Lyne, A. G., & Lorimer, D. R. (1994, May). High birth velocities of radio pulsars. , *369*(6476), 127-129. doi: 10.1038/369127a0

Madau, P., & Fragos, T. (2017, May). Radiation Backgrounds at Cosmic Dawn: X-Rays from Compact Binaries. *Astrophysical Journal*, *840*(1), 39. doi: 10.3847/1538-4357/aa6af9

Maeder, A., & Meynet, G. (2000, January). The Evolution of Rotating Stars. , *38*, 143-190. doi: 10.1146/annurev.astro.38.1.143

Marchant, P., Pappas, K. M. W., Gallegos-Garcia, M., Berry, C. P. L., Taam, R. E., Kalogera, V., & Podsiadlowski, P. (2021, June). The role of mass transfer and common envelope evolution in the formation of merging binary black holes. *Astronomy & Astrophysics*, *650*, A107. doi: 10.1051/0004-6361/202039992

Marigo, P., Chiosi, C., & Kudritzki, R. P. (2003, February). Zero-metallicity stars. II. Evolution of very massive objects with mass loss. *Astronomy & Astrophysics*, *399*, 617-630. doi: 10.1051/0004-6361:20021756

Marigo, P., Girardi, L., Chiosi, C., & Wood, P. R. (2001, May). Zero-metallicity stars. I. Evolution at constant mass. *Astronomy & Astrophysics*, *371*, 152-173. doi: 10.1051/0004-6361:20010309

McKee, C. F., & Tan, J. C. (2008, July). The Formation of the First Stars. II. Radiative Feedback Processes and Implications for the Initial Mass Function. *Astrophysical Journal*, *681*(2), 771-797. doi: 10.1086/587434

Naoz, S., & Barkana, R. (2007, May). The formation and gas content of high-redshift galaxies and minihaloes. *Monthly Notices*, *377*(2), 667-676. doi: 10.1111/j.1365-2966.2007.11636.x

Ng, K. K. Y., Vitale, S., Farr, W. M., & Rodriguez, C. L. (2021, May). Probing Multiple Populations of Compact Binaries with Third-generation Gravitational-wave Detectors. , *913*(1), L5. doi: 10.3847/2041-8213/abf8be

O'Connor, E., & Ott, C. D. (2011, April). Black Hole Formation in Failing Core-Collapse Supernovae. *Astrophysical Journal*, *730*(2), 70. doi: 10.1088/0004-637X/730/2/70

Oh, S., Kroupa, P., & Pflamm-Altenburg, J. (2015, June). Dependency of Dynamical Ejections of O Stars on the Masses of Very Young Star Clusters. *Astrophysical Journal*, *805*(2), 92. doi: 10.1088/0004-637X/805/2/92

Ohkubo, T., Nomoto, K., Umeda, H., Yoshida, N., & Tsuruta, S. (2009, December). Evolution of Very Massive Population III Stars with Mass Accretion from Pre-main Sequence to Collapse. *Astrophysical Journal*, *706*(2), 1184-1193. doi: 10.1088/0004-637X/706/2/1184

Omukai, K., & Palla, F. (2003, June). Formation of the First Stars by Accretion. *Astrophysical Journal*, *589*(2), 677-687. doi: 10.1086/374810

Paczynski, B. (1976, January). Common Envelope Binaries. In P. Eggleton, S. Mitton, & J. Whelan (Eds.), *Structure and evolution of close binary systems* (Vol. 73, p. 75).

Pallottini, A., Ferrara, A., Gallerani, S., Salvadori, S., & D'Odorico, V. (2014, May). Simulating cosmic metal enrichment by the first galaxies. *Monthly Notices*, *440*(3), 2498-2518. doi: 10.1093/mnras/stu451

Peebles, P. J. E. (1993). *Principles of Physical Cosmology.*

Peters, P. C. (1964, November). Gravitational Radiation and the Motion of Two Point Masses. *Physical Review*, *136*(4B), 1224-1232. doi: 10.1103/PhysRev.136.B1224

Peters, T., Klessen, R. S., Mac Low, M.-M., & Banerjee, R. (2010, December). Limiting Accretion onto Massive Stars by Fragmentation-induced Starvation. *Astrophysical Journal*, *725*(1), 134-145. doi: 10.1088/0004-637X/725/1/134

Pinsonneault, M. H., & Stanek, K. Z. (2006, March). Binaries Like to Be Twins: Implications for Doubly Degenerate Binaries, the Type Ia Supernova Rate, and Other Interacting Binaries. , *639*(2), L67-L70. doi: 10.1086/502799

Planck Collaboration, Ade, P. A. R., Aghanim, N., Arnaud, M., Ashdown, M., Aumont, J., ... Zonca, A. (2016, September). Planck 2015 results. XIII. Cosmological parameters. *Astronomy & Astrophysics*, *594*, A13. doi: 10.1051/0004-6361/201525830

Planck Collaboration, Aghanim, N., Akrami, Y., & Ashdown, M. e. a. (2020, September). Planck 2018 results. VI. Cosmological parameters. *Astronomy & Astrophysics*, *641*, A6. doi: 10.1051/0004-6361/201833910

Punturo, M., Abernathy, M., & Acernese, F. e. a. (2010, October). The Einstein Telescope: a third-generation gravitational wave observatory. *Classical and Quantum Gravity*, *27*(19), 194002. doi: 10.1088/0264-9381/27/19/194002

Rees, M. J., & Ostriker, J. P. (1977, June). Cooling, dynamics and fragmentation of massive gas clouds: clues to the masses and radii of galaxies and clusters. *Monthly Notices*, *179*, 541-559. doi: 10.1093/mnras/179.4.541

Reitze, D., Adhikari, R. X., Ballmer, S., Barish, B., Barsotti, L., Billingsley, G., ... Zucker, M. (2019, September). Cosmic Explorer: The U.S. Contribution to Gravitational-Wave Astronomy beyond LIGO. In *Bulletin of the american astronomical society* (Vol. 51, p. 35).

Ripamonti, E., & Abel, T. (2004, March). Fragmentation and the formation of primordial protostars: the possible role of collision-induced emission. *Monthly Notices*, *348*(3), 1019-1034. doi: 10.1111/j.1365-2966.2004.07422.x

Robson, T., Cornish, N. J., & Liu, C. (2019, May). The construction and use of LISA sensitivity curves. *Classical and Quantum Gravity*, *36*(10), 105011. doi: 10.1088/1361-6382/ab1101

Salpeter, E. E. (1955, January). The Luminosity Function and Stellar Evolution. *Astrophysical Journal*, *121*, 161. doi: 10.1086/145971

Sana, H., de Koter, A., de Mink, S. E., Dunstall, P. R., Evans, C. J., Hénault-Brunet, V., ... Vink, J. S. (2013, February). The VLT-FLAMES Tarantula Survey. VIII. Multiplicity properties of the O-type star population. *Astronomy & Astrophysics*, *550*, A107. doi: 10.1051/0004-6361/201219621

Sana, H., de Mink, S. E., de Koter, A., Langer, N., Evans, C. J., Gieles, M., ... Schneider, F. R. N. (2012, July). Binary Interaction Dominates the Evolution of Massive Stars. *Science*, *337*(6093), 444. doi: 10.1126/science.1223344

Santoliquido, F., Mapelli, M., Bouffanais, Y., Giacobbo, N., Di Carlo, U. N., Rastello, S., ... Ballone, A. (2020, August). The Cosmic Merger Rate Density Evolution of Compact Binaries Formed in Young Star Clus-

ters and in Isolated Binaries. *Astrophysical Journal*, *898*(2), 152. doi: 10.3847/1538-4357/ab9b78

Sarmento, R., Scannapieco, E., & Cohen, S. (2018, February). Following the Cosmic Evolution of Pristine Gas. II. The Search for Pop III-bright Galaxies. *Astrophysical Journal*, *854*(1), 75. doi: 10.3847/1538-4357/aa989a

Sathyaprakash, B. S., & Schutz, B. F. (2009, December). Physics, Astrophysics and Cosmology with Gravitational Waves. *Living Reviews in Relativity*, *12*(1), 2. doi: 10.12942/lrr-2009-2

Schneider, R., Ferrara, A., Natarajan, P., & Omukai, K. (2002, May). First Stars, Very Massive Black Holes, and Metals. *Astrophysical Journal*, *571*(1), 30-39. doi: 10.1086/339917

Schneider, R., Ferrara, A., Salvaterra, R., Omukai, K., & Bromm, V. (2003, April). Low-mass relics of early star formation. , *422*(6934), 869-871. doi: 10.1038/nature01579

Schneider, R., Omukai, K., Inoue, A. K., & Ferrara, A. (2006, July). Fragmentation of star-forming clouds enriched with the first dust. *Monthly Notices*, *369*(3), 1437-1444. doi: 10.1111/j.1365-2966.2006.10391.x

Schwarzschild, M., & Spitzer, L. (1953, April). On the evolution of stars and chemical elements in the early phases of a galaxy. *The Observatory*, *73*, 77-79.

Skinner, D., & Wise, J. H. (2020, March). Cradles of the first stars: self-shielding, halo masses, and multiplicity. *Monthly Notices*, *492*(3), 4386-4397. doi: 10.1093/mnras/staa139

Spera, M., Mapelli, M., Giacobbo, N., Trani, A. A., Bressan, A., & Costa, G. (2019, May). Merging black hole binaries with the SEVN code. *Monthly Notices*, *485*(1), 889-907. doi: 10.1093/mnras/stz359

Stacy, A., & Bromm, V. (2013, August). Constraining the statistics of Population III binaries. *Monthly Notices*, *433*(2), 1094-1107. doi: 10.1093/mnras/stt789

Stacy, A., & Bromm, V. (2014, April). The First Stars: A Low-mass Formation Mode. *Astrophysical Journal*, *785*(1), 73. doi: 10.1088/0004-637X/785/1/73

Susa, H., Hasegawa, K., & Tominaga, N. (2014, September). The Mass Spectrum of the First Stars. *Astrophysical Journal*, *792*(1), 32. doi: 10.1088/0004-637X/792/1/32

Tanikawa, A., Chiaki, G., Kinugawa, T., Suwa, Y., & Tominaga, N. (2022, February). Can Population III stars be major origins of both merging binary black holes and extremely metal poor stars? *arXiv e-prints*, arXiv:2202.00230.

Tanikawa, A., Susa, H., Yoshida, T., Trani, A. A., & Kinugawa, T. (2021, March). Merger Rate Density of Population III Binary Black Holes Below, Above, and in the Pair-instability Mass Gap. *Astrophysical Journal*, *910*(1), 30. doi: 10.3847/1538-4357/abe40d

Tanikawa, A., Yoshida, T., Kinugawa, T., Takahashi, K., & Umeda, H. (2020, July). Fitting formulae for evolution tracks of massive stars under extreme metal-poor environments for population synthesis calculations

and star cluster simulations. *Monthly Notices*, *495*(4), 4170-4191. doi: 10.1093/mnras/staa1417

Tanikawa, A., Yoshida, T., Kinugawa, T., Trani, A. A., Hosokawa, T., Susa, H., & Omukai, K. (2022, February). Merger Rate Density of Binary Black Holes through Isolated Population I, II, III and Extremely Metal-poor Binary Star Evolution. *Astrophysical Journal*, *926*(1), 83. doi: 10.3847/1538-4357/ac4247

Tegmark, M., Silk, J., Rees, M. J., Blanchard, A., Abel, T., & Palla, F. (1997, January). How Small Were the First Cosmological Objects? *Astrophysical Journal*, *474*, 1. doi: 10.1086/303434

The LIGO Scientific Collaboration, the Virgo Collaboration, the KAGRA Collaboration, Abbott, R., Abbott, T. D., Acernese, F., ... Zweizig, J. (2021, November). GWTC-3: Compact Binary Coalescences Observed by LIGO and Virgo During the Second Part of the Third Observing Run. *arXiv e-prints*, arXiv:2111.03606.

Tornatore, L., Ferrara, A., & Schneider, R. (2007, December). Population III stars: hidden or disappeared? *Monthly Notices*, *382*(3), 945-950. doi: 10.1111/j.1365-2966.2007.12215.x

Turk, M. J., Abel, T., & O'Shea, B. (2009, July). The Formation of Population III Binaries from Cosmological Initial Conditions. *Science*, *325*(5940), 601. doi: 10.1126/science.1173540

Valiante, R., Schneider, R., Volonteri, M., & Omukai, K. (2016, April). From the first stars to the first black holes. *Monthly Notices*, *457*(3), 3356-3371. doi: 10.1093/mnras/stw225

Wagner, R. L. (1978, January). Theoretical evolution of extremely metal-poor stars. II. *Astronomy & Astrophysics*, *62*(1-2), 9-12.

Webbink, R. F. (1984, February). Double white dwarfs as progenitors of R Coronae Borealis stars and type I supernovae. *Astrophysical Journal*, *277*, 355-360. doi: 10.1086/161701

Windhorst, R. A., Timmes, F. X., Wyithe, J. S. B., Alpaslan, M., Andrews, S. K., Coe, D., ... Kim, D. (2018, February). On the Observability of Individual Population III Stars and Their Stellar-mass Black Hole Accretion Disks through Cluster Caustic Transits. , *234*(2), 41. doi: 10.3847/1538-4365/aaa760

Wise, J. H., Demchenko, V. G., Halicek, M. T., Norman, M. L., Turk, M. J., Abel, T., & Smith, B. D. (2014, August). The birth of a galaxy - III. Propelling reionization with the faintest galaxies. *Monthly Notices*, *442*(3), 2560-2579. doi: 10.1093/mnras/stu979

Woosley, S. E., & Heger, A. (2015, January). The Deaths of Very Massive Stars. In J. S. Vink (Ed.), *Very massive stars in the local universe* (Vol. 412, p. 199). doi: 10.1007/978-3-319-09596-7_7

Woosley, S. E., & Weaver, T. A. (1986, January). The physics of supernova explosions. , *24*, 205-253. doi: 10.1146/annurev.aa.24.090186.001225

Woosley, S. E., & Weaver, T. A. (1995, November). The Evolution and Explosion of Massive Stars. II. Explosive Hydrodynamics and Nucleosynthesis. , *101*, 181. doi: 10.1086/192237

Wyithe, J. S. B., & Loeb, A. (2003, April). Reionization of Hydrogen and Helium by Early Stars and Quasars. *Astrophysical Journal*, *586*(2), 693-708. doi: 10.1086/367721

Xu, H., Norman, M. L., O'Shea, B. W., & Wise, J. H. (2016, June). Late Pop III Star Formation During the Epoch of Reionization: Results from the Renaissance Simulations. *Astrophysical Journal*, *823*(2), 140. doi: 10.3847/0004-637X/823/2/140

Yoon, S. C., Dierks, A., & Langer, N. (2012, June). Evolution of massive Population III stars with rotation and magnetic fields. *Astronomy & Astrophysics*, *542*, A113. doi: 10.1051/0004-6361/201117769

Yoshida, N., Bromm, V., & Hernquist, L. (2004, April). The Era of Massive Population III Stars: Cosmological Implications and Self-Termination. *Astrophysical Journal*, *605*(2), 579-590. doi: 10.1086/382499

Yoshida, N., Omukai, K., & Hernquist, L. (2008, August). Protostar Formation in the Early Universe. *Science*, *321*(5889), 669. doi: 10.1126/science.1160259